Demonstrating Quantum Speed-Up with a Two-Transmon Quantum Processor.

Andreas Dewes

April 22, 2012

Contents

List of Figures

List of Tables

Chapter 1

Introduction & Summary

1.1 Quantum Computing & Circuit Quantum Electrodynamics

This thesis presents experiments performed with a superconducting two-qubit quantum processor. The main goal of this work was to demonstrate a possible quantum computing architecture using superconducting qubits that follows the canonical blueprint of a quantum processor as shown in fig. 1.1, following the four criteria formulated by DiVincenzo (2000). Following this definition, a universal quantum computer is a register of quantum bits – or qubits – on which one can perform universal single- and two-qubit quantum gates, read out the state of each qubit individually and with high fidelity and reset the qubit register to a well-defined state.

Implementing this allegedly simple list of requirements in a system of superconducting qubits has been a major research challenge during the last decade. The first demonstration of coherent quantum dynamics in a superconducting charge-based qubit by Nakamura et al. (1999) opened up a broad research field on superconducting quantum bits. In the years following Nakamuras initial experiment, several types of super-
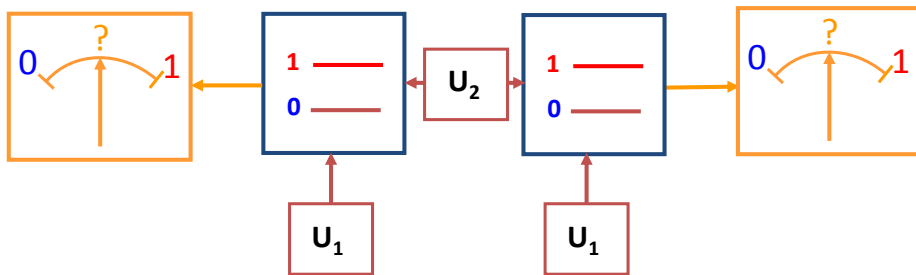

Figure 1.1: The blueprint of a two-qubit quantum processor. Shown are two qubits that can be individually manipulated (U_1) and are connected by a universal two-qubit gate U_2. Each of the qubits can be read out individually.

conducting qubits were proposed and realized using e.g. the superconducting phase (Martinis et al., 1985, 2002) across a Josephson junction or the magnetic flux (Mooij et al., 1999; Chiorescu et al., 2003) inside a superconducting ring interrupted by one or several Josephson junctions as the dominant quantum variable. An important result on the way to the development of robust superconducting qubits was the development of the so-called *Quantronium* qubit by Vion et al. (2002), which achieved quantum-mechanical coherence times larger than 1 μs, made possible by operating a Cooper pair box at a sweet spot in a regime where the charging and Josephson phase energies of the system are of comparable value. The high coherence times achieved with this qubit made it possible to perform –for the first time– robust, NMR-like quantum operations using a superconducting qubit (Collin et al., 2004). Then, in 2004, the development of a new type of qubit, the so called *Transmon* by Wallraff et al. (2004) marked again a drastic improvement in coherence times. By decreasing the charging energy of a Cooper pair box and thus operating the device in the phase regime, the resulting qubit becomes quasi insensitive to charge noise. Furthermore, by embedding the Transmon qubit in a superconducting coplanar waveguide (CPW) resonator it is possible to protect it from external sources of electrical noise and to use the dirspersive interaction between the qubit and the resonator for reading out the qubit state(Blais et al., 2004). With this so-called *circuit quantum electrodyanmics* (CQED) architecture, quantum gates and algorithms with up to three qubits have been implemented so-far, demonstrating multi-qubit entanglement (DiCarlo et al., 2010) and simple quantum algorithms (DiCarlo et al., 2009).

!1!

In parallel to this, the development of reliable quantum-limited amplifiers based on nonlinear superconducting resonators by ?1? I. Siddiqi (Siddiqi et al., 2004; Vijay et al., 2009) complemented the CQED architecture by providing a fast and high-fidelity readout scheme for Transmon qubits (Siddiqi et al., 2006; Mallet et al., 2009) and for the amplification of quantum signals in general !2! . These quantum-limited amplifiers and detectors made it possible to directly observe quantum jumps in superconducting qubits (Vijay et al., 2011) and to implement simple quantum feedback schemes in superconducting circuits !3! .

Recently, the development of a CQED architecture combining Transmon qubits with 3D superconducting resonator cavities instead of 1D coplanar waveguide resonators, as pioneered by Paik et al. (2011), resulted in an increase of qubit lifetimes of almost two orders of magnitude, with measured T_1 qubit relaxation times as high as $80 \ \mu s$!4! and decoherence times at a comparable time scale. This increase in coherence times made possible the realization of high-fidelity quantum gates and qubit readout schemes !5! as well as elemental quantum feedback and error correction schemes, thus providing another promising route to quantum computation with superconducting qubits. !6!

The research presented in this thesis aims to complement the CQED architecture by

To Do 1: Think about moving the section on 3D-CQED directly after this one since this would probably be more logical

Question 1: Should I mention Michel here?

To Do 2: Add more citations here

To Do 3: Add reference to quantum feedback paper as soon as it appears

To Do 4: verify this!

To Do 5: add references!

To Do 6: expand this section as soon as new relevant material appears, include recent IBM, Yale

combining a multi-qubit architecture with a single-shot, individual-qubit readout scheme, thus aiming to develop a viable architecture for the implementation of a superconducting quantum computer using Transmon qubits.

The first part of the thesis discusses the realization of a superconducting quantum processor with Transmon qubits that are fitted with individual-qubit, single-shot readouts. We demonstrate elementary one- and two-qubit quantum operations with this processor and use it to implement a simple quantum algorithm that demonstrates probabilistic quantum speed-up at the two-qubit level. Finally, we discuss the realization of a four-qubit quantum processor with a more scalable architecture that could possibly be extended to an even larger number of qubits.

1.2 Realizing a Two-Qubit Quantum Processor
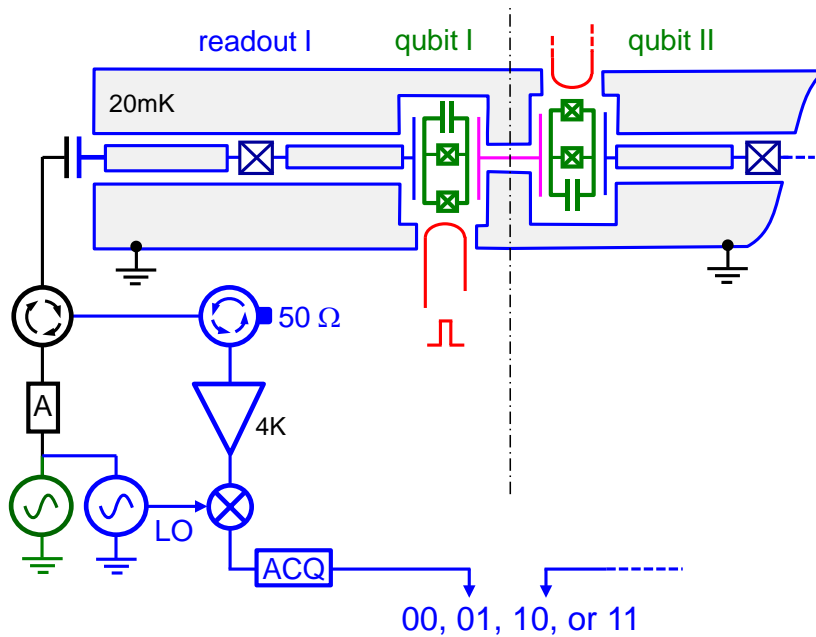
Figure 1.2: Circuit schematic of the two-qubit processor realized in this work, showing the two qubits in green, the qubit readouts in blue and the fast flux lines in red. Each qubit is embedded in its own nonlinear readout resonator and can be driven and read out through an individual microwave line.

The quantum processor implemented in this work is shown in fig. 1.2. It consists of two superconducting quantum bits of the Transmon-type, each equipped with its own drive and readout circuit. The qubit readout is realized by using a nonlinear coplanar-waveguide resonator which serves as a cavity bifurcation amplifier (CBA)(Vijay et al., 2009) and implements a single-shot readout of the qubit state. Each qubit can be manipulated by driving it with microwave pulses through its readout resonator, allowing robust

and fast single-qubit operations. The qubit frequencies can be tuned individually by fast flux lines, which allows to change the frequency each qubit over a range of several GHz. The coupling between the two qubits is realized through a fixed capacitance that connects the two top-electrodes of the qubits and implements a fixed σ_{xx}-type qubit-qubit coupling. This coupling allows us to implement a two-qubit gate and to generate entangled two-qubit states. We use this simple processor to test Bell's inequality, implement an universal two-qubit gate and perform a simple quantum algorithm that demonstrates probabilistic quantum speed-up, as will be discussed in the following sections.

1.3   Demonstrating Simultaneous Single-Shot Readout
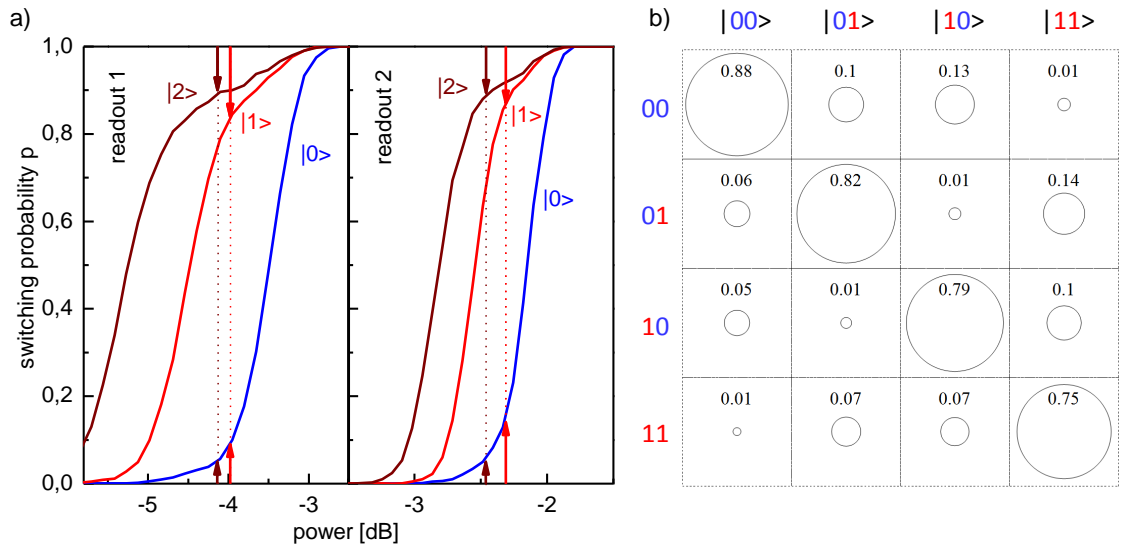
Figure 1.3: a) Switching probabilities of the two qubit readouts as a function of the readout excitation power. The measurement is performed after preparing the qubits in the states $|0\rangle$, $|1\rangle$ and $|2\rangle$. The readout fidelity is given as the difference in probability between the curves corresponding to the states $|0\rangle$ and $|1\rangle$ or $|2\rangle$, respectively. The highest readout fidelites of 88 and 89 % are achieved when the qubit is in state $|2\rangle$. b) Readout matrix of the two-qubit system. The matrix contains the probabilities of obtaining a given measurement result after having prepared the system in a given state.   Figure Comment 2: Replace this figure since it is not very intuitive. It would be better to show something which allows the reader to directly quantify the visibility and readout crosstalk present in the system.

To read out the state of each qubit, a so-called cavity bifurcation amplifier (Siddiqi et al., 2006; Mallet et al., 2009) is used. This readout technique works by capacitively coupling the qubit to a coplanar waveguide resonator which is rendered nonlinear by a Josephson junction placed in its center conductor. This nonlinear resonator can exhibit hysteretic behaviour for certain drive parameters, which can be used to map the state of the qubit to one of the bistable states of the resonator, thereby obtaining a single-shot

readout. Contrary to other CQED approaches, in our setup each qubit is fitted with an individual CBA readout, allowing thus a simultaneous measurement of the full two-qubit register and therefore following closely the canonical blueprint of a quantum computer as formulated by DiVincenzo. !7! Readout fidelitis up to 93 % have been demonstrated using the CBA readout technique (Mallet et al., 2009) but due to design contraints only 83-85 % fidelity have been attained in our experiments. The full characterization of the two-qubit readout is shown in fig. 1.3. Fig. 1.3a shows the so-called s curves of each qubit readout, which shown the working-point dependent switching probabilities of each readout with the qubits in different states. Fig. 1.3b shows the full readout matrix, which connects readout switching probabilities with qubit state occupation probabilities and allows for the correction of all readout errors.

To Do 7: discuss more details of the readout here...

1.4 Generating and Characterizing Entanglement

The fixed coupling between the two qubits provides a σ_{xx}-type coupling which is only effective when the qubit frequencies are nearly resonant. Therefore, it can be switched on and off by changing the qubit frequencies, which we use to implement two-qubit gates with this system. In our processor, the effective coupling constant g of the two qubits is given as $2g = 8.2 \ \mathrm{MHz}$!8! . When using a fast fluxline pulse to abruptly tune the qubits in resonance we can switch on the qubit-qubit coupling non-adiabatically and generate an evolution operator of the form

To Do 8: Check if this is really $2g$!

$$U(t) = \begin{pmatrix} 1 & 0 & 0 & 0 \\ 0 & \cos 2\pi tg & i\sin 2\pi tg & 0 \\ 0 & i\sin 2\pi tg & \cos 2\pi tg & 0 \\ 0 & 0 & 0 & 1 \end{pmatrix} \tag{1.1}$$

Switching off this interaction after a time $t_{\pi/2} = 1/8g$ allows the creation of entangled qubit states and the implementation of a universal quantum gate, as will be explained later. Before doing this, we characterize the evoluation of the qubits during the swapping interaction by preparing them in the state $|10\rangle$, switching on the interaction for a given amount of time and measuring the qubit state directly afterwards. The resulting curve shown in fig. 1.4 shows energy oscillations between the two qubits. Stopping the interaction after quarter of a period we obtain an entangled two-qubit Bell-type state that we can characterize by performing quantum state tomography. The experimental reconstruction of the density matrix of such a state corresponding approximating to the Bell-state $|\psi\rangle = 1/\sqrt{2}(|01\rangle + i\,|10\rangle)$ is shown in fig. 1.4b. The measured fidelity of this state of 91 % and the concurrence of 85 % confirms that entanglement is present in the system. This entanglement can also be characterized by measuring the so-called
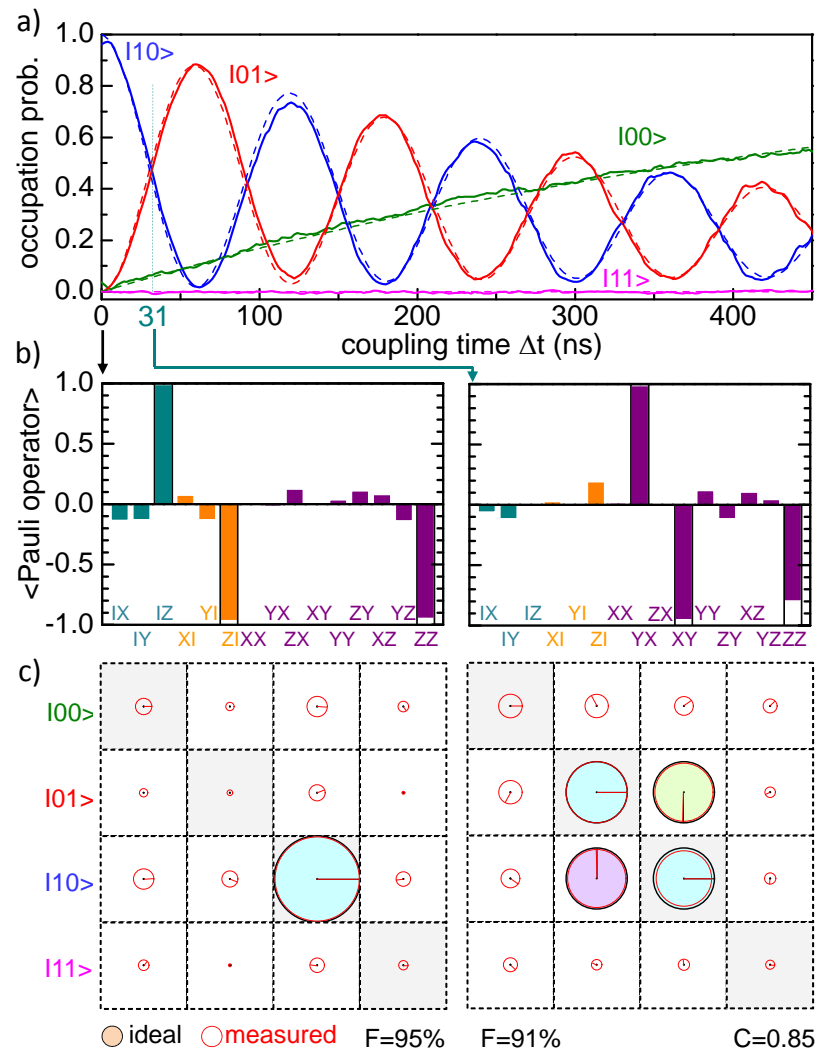
Figure 1.4: Energy oscillations between the two qubits induced by a resonant swapping interaction between them. a) The qubit state after switching on the swapping interaction for a given time Δt. The frequency of the oscillations corresponds to $2g = 8.7$ MHz. b) The Pauli set of the two-qubit state measured at 0 ns and 31 ns. c) The reconstructed density matrices corresponding to the two measured Pauli sets. In c), the area of each circle corresponds to the absolute value of each matrix element and the color and direction of the arrow give the phase of each element. The black circles correspond to the density matrices of the ideal states $|10\rangle$ and $1/\sqrt{2}/(|10\rangle + i\,|01\rangle)$, respectively. Figure Comment 4: verify sign!

Clauser-Horne-Shimony-Holt operator (Clauser et al., 1969) on the produced state. This operator is given as

$$\mathrm{CHSH} = \mathrm{QS} + \mathrm{RS} + \mathrm{RT} - \mathrm{QT} \qquad (1.2)$$

with the operators $\mathrm{Q}, \mathrm{R}, \mathrm{S}, \mathrm{T}$ being given as

$$
\begin{aligned}
\mathrm{Q} &= \sigma_z^1 & \mathrm{S} &= \sigma_z^2 \cdot \cos\phi + \sigma_x^2 \cdot \sin\phi \\
\mathrm{R} &= \sigma_x^1 & \mathrm{T} &= -\sigma_z^2 \cdot \sin\phi + \sigma_x^2 \cdot \cos\phi
\end{aligned} \qquad (1.3)
$$

Here, the angle ϕ is a parameter that should be chosen in accordance to the phase of the Bell state on which the operator is applied.
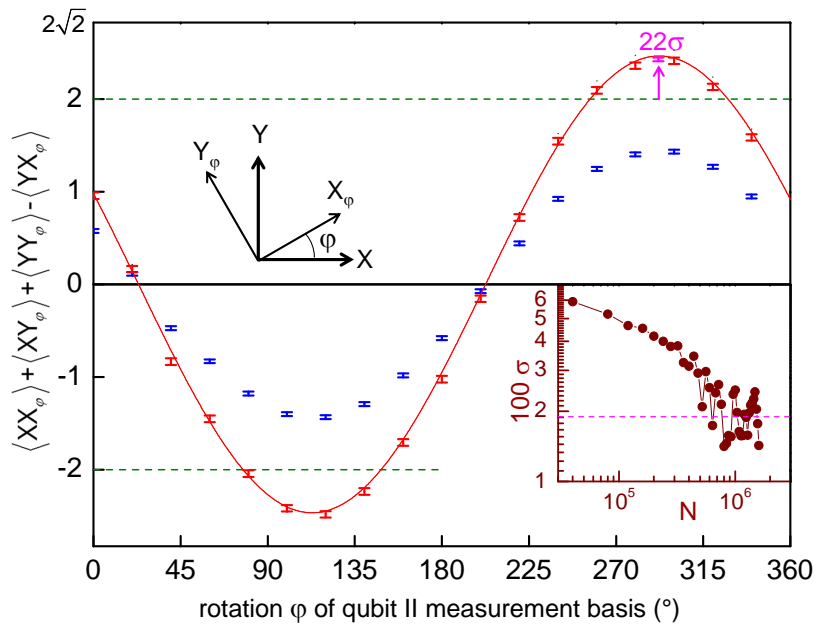
Figure 1.5: Measurement of the CHSH equation for an entangled two-qubit state. The renormalized CHSH expectation value (red points) exceeds the classical boundary of 2 by a large amount. The raw measurement data (blue points) lies below this critical threshold. The inset shows the standard deviation σ at the highest point of the curve as a function of the measurement sample size. For the highest sample count, the classical boundary is exceeded by 22 standard deviations. Figure Comment 6: p. 140 in cavities 6 labbook

The expectation value $\langle CHSH \rangle$ provides a test of the quantum-mechanical character of the generated state. For classical states, the maximum value is ≤ 2 but for entangled states it can reach a maximum value of $\sqrt{2} \cdot 2$. The result of a CHSH-type measurement performed on a state created by the method described above is shown in fig. 1.5, showing the value of $\langle CHSH \rangle$ as a function of ϕ. We observe a violation of the classical boundary 2 of the operator by 22 standard deviations when correcting readout errors present in our system. However, the raw, uncorrected data fails to exceed

the non-classical bound, making it impossible to close the detection loophole with our system. Nevertheless the observed violation of the equation by the renormalized state is a strong indication of entanglement in the system.

1.5 Realizing a Universal Two-Qubit Quantum Gate

Figure 1.6: The measured χ-matrix of the implemented $\sqrt{i\mathrm{SWAP}}$ gate. The row labels correspond to the indices of the E_i operators, the height of each bar to the absolute value of the corresponding matrix element and the color and direction of the red arrow to the complex phase of each element. The ideal χ-matrix of the $i\sqrt{\mathrm{SWAP}}$ gate is given by the outlined bars. The upper half of the positive-hermitian matrix is not shown.
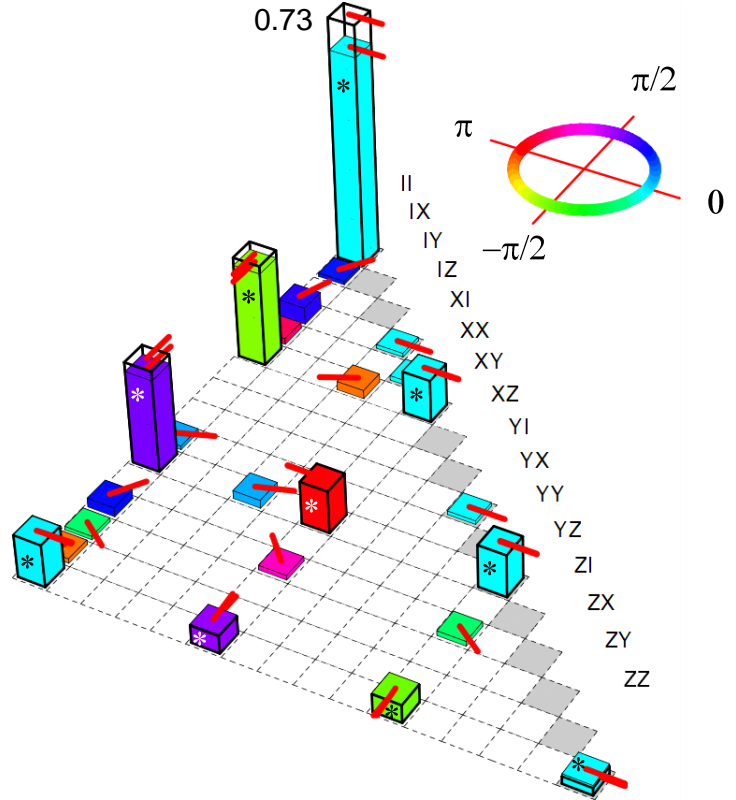
The swapping evolution according to eq. (1.1) allows the implementation of a two-qubit gate. When switching on this interaction for $t_{\pi/2} = 1/8g$ we can realize the so-called $\sqrt{i\mathrm{SWAP}}$ gate, which has the representation

$$\sqrt{i\mathrm{SWAP}} = \begin{pmatrix} 1 & 0 & 0 & 0 \\ 0 & 1/\sqrt{2} & i/\sqrt{2} & 0 \\ 0 & i/\sqrt{2} & 1/\sqrt{2} & 0 \\ 0 & 0 & 0 & 1 \end{pmatrix} \tag{1.4}$$

and is a universal two-qubit quantum gate. The operation and errors of our implementation of this gate can be characterized by performing quantum process tomography, yielding a gate fidelity of 90 % . The 10 % error in gate fidelity is caused mainly by qubit relaxation and dephasing during the gate operation and only marginally by deterministic preparation errors, as will be discussed in the main text of the thesis. Fig. 1.6 show

the measured χ matrix of the implemented gate. The achieved fidelity of the gate operation is sufficient to allow the implementation of a simple quantum algorithm with our processor, as will be discussed in the following section.

1.6 Running a Quantum-Search Algorithm
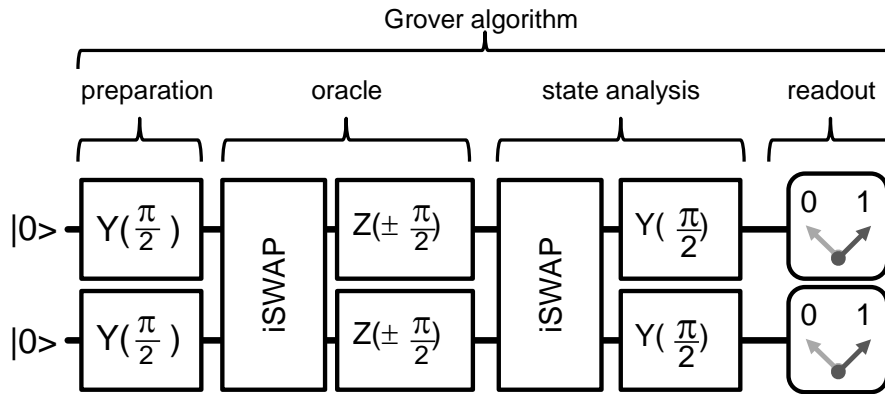
Figure 1.7: Schematic of the implementation of Grovers search algorithm on a two-qubit quantum processor. The algorithm consists in preparing a probe state, applying the quantum oracle to this state and analyzing the resulting output state to extract the information on the oracle operator.

In this work we use the quantum gate implemented above to run a compiled version of Grover's search algorithm (Grover, 1997). The implemented version of the algorithm works in the basis of two qubits $x_i \in \{|00\rangle, |01\rangle, |10\rangle, |11\rangle\}$ and can distinguish between four different *oracle functions* $f(x)$ that each tag on one of the basis states x_j. Since the Grover algorithm for 2 qubits requires only one evaluation of the function $f(x)$ to determine which state has been marked it is faster than any conceivable classical algorithm, thus demonstrating the concept of quantum speed-up. The schematic of our version of Grover's algorithm is shown in fig. 1.7 and involves two $i\mathrm{SWAP}$ gates and three single-qubit operations along with a single-shot qubit readout at the end of the algorithm. We implemented all steps of this algorithm with our two-qubit processor and performed quantum state tomography after each step to reconstruct the quantum state at different points in the algorithm. Fig. 1.8 shows the experimentially measured density matrices when running the algorithm with an oracle that marks the state $|00\rangle$. State tomographies are shown after applying the generalized Hadamard transform, after applying the quantum oracle and after the final step of the algorithm. This reconstruction of the quantum state using quantum state tomography does not however allow to demonstrate quantum speed-up, which requires individual single-shot readout of the qubit register, which will be discussed in the following section.
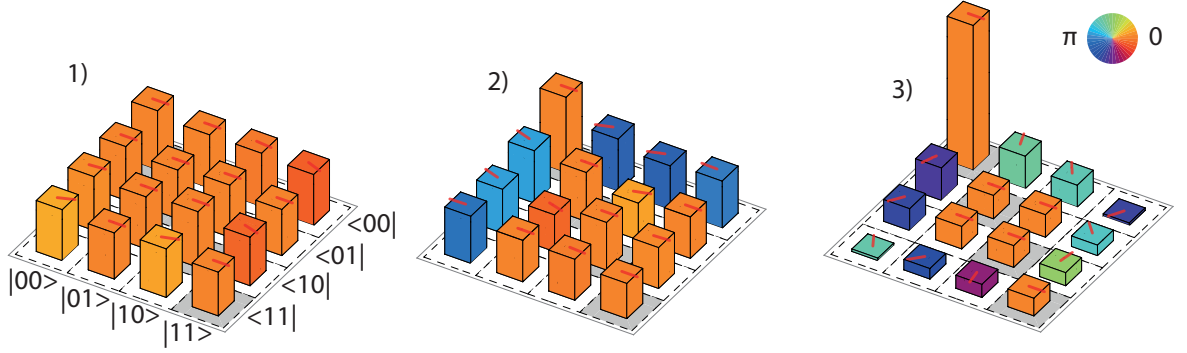
Figure 1.8: Measured density matrices when running Grover's search algorithm with a search oracle marking the state $|00\rangle$. 1) shows the state after the generalized Hadamard transform, 2) after applying the quantum oracle and 3) after the final step of Grover's algorithm.

1.7   Demonstrating Quantum Speed-Up

The main interest of running a quantum algorithm is to obtain an advantage in the run-time in comparision with a classical algorithm, the so-called *quantum speed-up*. To characterize this quantum speed-up as obtained with our processor, we run Grovers algorithm for all four possible oracle functions and directly readout out the qubit state after the last step of the algorithm, without correcting any readout errors. When averaging the results of such individual runs of the algorithm we can then obtain its single-run fidelity, which –for our processor– ranges between 52 and 67 %, depending on the state which is marked by the quantum oracle, as shown in fig. 1.9. These results clearly demonstrate quantum speed-up in this system, although the achieved success probability is considerably lower than the theoretically possible value of 100 % . The reduced fidelity is mainly due to relaxation and decoherence of the qubit state during the running of the algorithm and to a very small degree due to errors in the pulse sequence and drifts in the measurement equipment.

1.8   Designing a Scalable Quantum Computing Architecture

After having demonstrated the different building blocks of a superconducting, Transmon-based quantum processor it remains to be shown that larger-scale quantum-computing beyond two qubits is possible with this system. This work therefore pursued the realization of a more scalable qubit architecture using systems of up to six qubits coupled through a so-called "quantum bus" (Majer et al., 2007). The details of this novel architecture are discussed in the following sections.
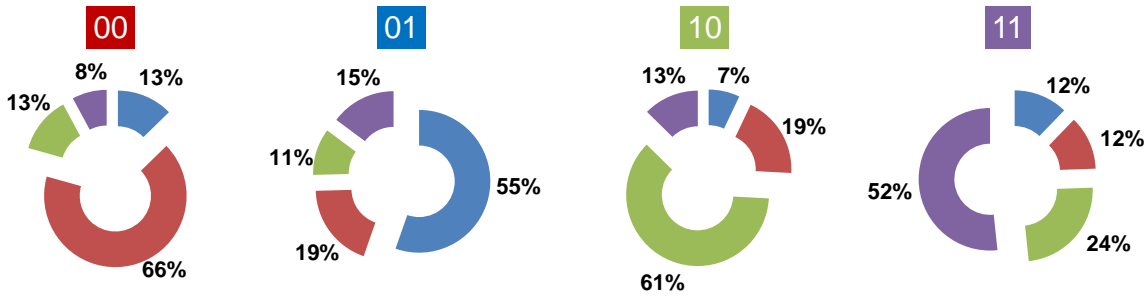
Figure 1.9: Single-run results when running the Grover search algorithm on our two-qubit quantum processor. Shown are the probabilities of obtaining the results $00, 01, 10, 11$ as a function of the oracle function provided to the algorithm, indicated by the number on top of each graph. In all four cases, the success probability of the algorithm is $> 50\%$, thus outperforming any classical algorithm in the number of calls to the oracle function.

The approach for scalable quantum computing with superconducting qubits pursued in this work consists of a system of many individual Transmon qubits equipped with individual JBA-based readouts, a multiplexed drive and readout circuit and a fixed qubit-qubit coupling mediated through a high-Q CPW resonator. As before, each qubit possesses a fluxline for fast frequency control. The readout and drive signals are send to all the qubits in parallel through a multiplexed transmission line. In this approach, the qubit and readout parameters, couplings and frequencies have to be carefully to avoid unwanted coupling between individual qubits and readouts and to allow the implementation of robust quantum gates between individual qubits. In this work we realized a 4-qubit chip and characterized it experimentally. The results of these experiments will be discussed in the main text of this thesis.
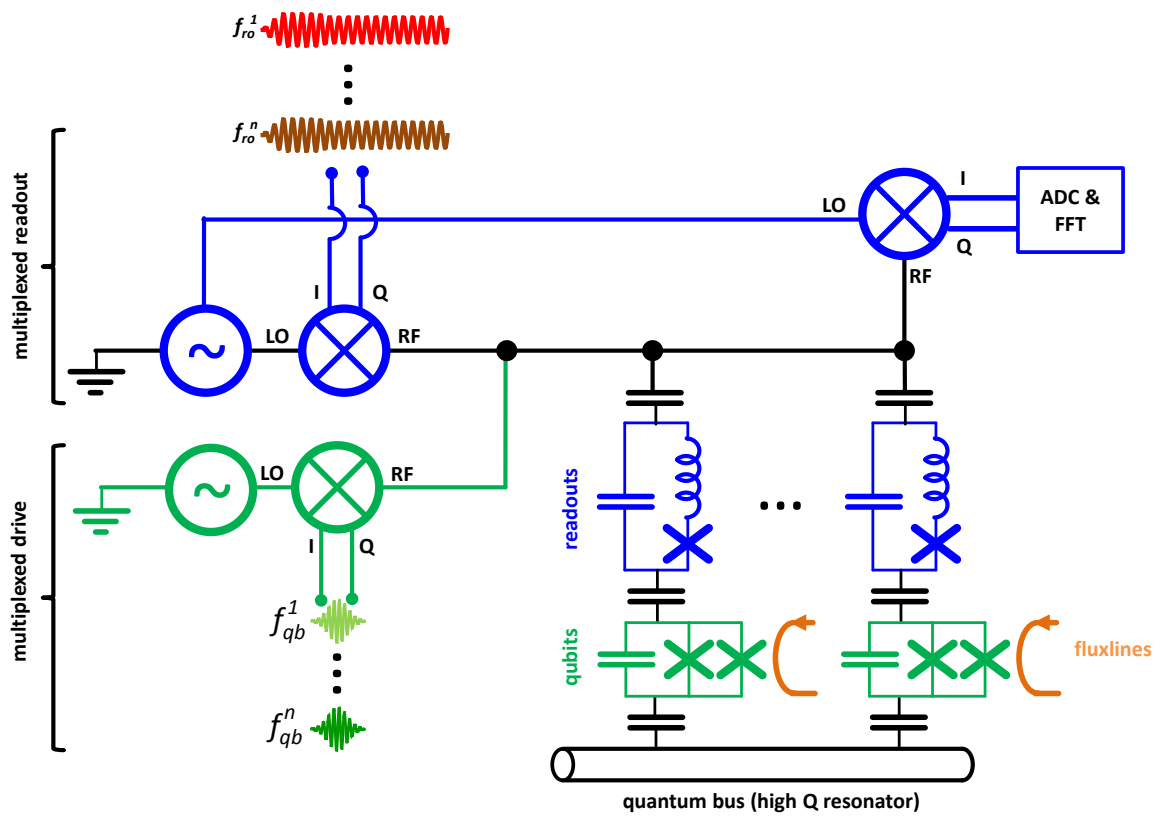
Figure 1.10: ...

Chapter 2

Theoretical Foundations

The goal of this chapter is to provide the theoretical foundations needed to interpret and analyze the experiments discussed in the following chapters. We will therefore briefly introduce some basic concepts of quantum mechanics and quantum computing, discuss Transmon qubits and circuit quantum electrodynamics (CQED) and introduce the reader to the Josephson bifurcation amplifier that we use to read out the qubit state in our experiments. Further details on all the elements discussed here will be provided in the relevant sections of the "Experiments" chapter.

2.1 Quantum mechanics & Quantum Computing

2.2 Transmon qubits

A Transmon qubit is essentially a Cooper pair box (CPB) operated in the phase regime, where $E_J \gg E_C$. The Hamiltionian of the CPB can be written as (Cottet, 2002)

$$\hat{H} = 4E_C \left(\hat{n} - n_g\right)^2 - E_J \cos \hat{\phi} \tag{2.1}$$

where $E_C = e^2/C_\Sigma$ is the charging energy with $C_\Sigma = C_J + C_B + C_g$ the total gate capacitance of the system, $\hat{n}$ is the number of Cooper pairs transferred between the islands, n_g the gate charge, E_J the Josephson energy of the junction and $\hat{\phi}$ the quantum phase across the junction.

This Hamiltonian can be solved exactly in the phase basis with the solutions being given as(Koch et al., 2007; Cottet, 2002)

$$E_m(n_g) = E_C a_{2[n_g+k(m,n_g)]}(-E_J/E_C) \tag{2.2}$$

Here, $a_\nu(q)$ denotes Mathieu's characteristic value and $k(m, n_g)$ is a function that sorts

the eigenvalues. We'll denote the energy differences between individual eigenstates by $E_{ij} = E_j - E_i$. The absolute anharmonicity of the first two Transmon transitions is given as $\alpha \equiv E_{12} - E_{01}$, the relative anharmonicity as $\alpha_r \equiv \alpha/E_{01}$. In the limit $E_J \gg E_C$ these are well approximated by $\alpha \simeq -E_C$ and $\alpha_r \simeq -(8E_J/E_C)^{-1/2}$.

2.3   Circuit quantum electrodynamics

For readout and noise protection, the Transmon qubit is usually coupled to a harmonic oscillator which is usually realized as a lumped-elements resonator or a coplanar waveguide resonator. In the limit where the resonator capacity $C_r \gg C_\Sigma$ we can write the effective Hamiltonian of the system as

$$\hat{H} = \hbar \sum_j \omega_j \left|j\right> \left<j\right| + \hbar\omega_r \hat{a}^\dagger \hat{a} + \hbar \sum_{i,j} g_{ij} \left|i\right> \left<j\right| (\hat{a} + \hat{a}^\dagger) \tag{2.3}$$

Here, $\omega_r = 1/\sqrt{L_r C_r}$ gives the resonator frequency and $\hat{a}$ ($\hat{a}^\dagger$) are annihilation (creation) operators acting on oscillator states. The voltage of the oscillator is given by $V_{rms}^0 = \sqrt{\hbar\omega_r/2C_r}$ and the parameter β gives the ratio between the gate capacitance and total capacitance, $\beta = C_g/C_\Sigma$. The coupling energies g_{ij} are given as

$$\hbar g_{ij} = 2\beta e V_{rms}^0 \left<i\right| \hat{n} \left|j\right> = \hbar g_{ji}^* \tag{2.4}$$

When the coupling between the resonator and the Transmon is weak $g_{ij} \ll \omega_r, E_{01}/h$ we can ignore the terms in eq. (2.3) that describe simultaneous excitation or deexcitation of the Transmon and the resonator and obtain a simpler Hamiltonian in the so-called *rotating wave approximation* given as

$$\hat{H} = \hbar \sum_j \omega_j \left|j\right> \left<j\right| + \hbar\omega_r \hat{a}^\dagger \hat{a} + \left(\hbar \sum_i g_{i,i+1} \left|i\right> \left<i+1\right| \hat{a}^\dagger + H.c.\right) \tag{2.5}$$

2.3.1   Dispersive limit & qubit readout

When the qubit frequency is far detuned from the resonator frequency direct qubit-resonator transition get exponentially supressed and the only interaction left between the two system is a dispersive shift of the transition frequencies. In this limit, the effective Hamiltonian of the system can be written as(Blais et al., 2004; Koch et al., 2007)

$$\hat{H}_{eff} = \frac{\hbar\omega_{01}'}{2}\hat{\sigma}_z + \hbar(\omega_r' + \chi\hat{\sigma}_z)\hat{a}^\dagger \hat{a} \tag{2.6}$$

Here, the resonance frequencies of both the qubit and the resonator are shifted and given as $\omega_r' = \omega_r - \chi_{12}/2$ and $\omega_{01}' = \omega_{01} + \chi_{01}$. The dispersive shift χ itself is given as

$$\chi = \chi_{01} - \chi_{12}/2 \tag{2.7}$$

$$\chi_{ij} = \frac{g_{ij}^2}{\omega_{ij} - \omega_r} = \frac{(2\beta e V_{rms}^0)^2}{\hbar^2 \Delta_i} |\langle i | \hat{n} | i+1 \rangle|^2 \tag{2.8}$$

The fact that χ_{01} and χ_{12} contribute to the total dispersive shift can cause the overall dispersive shift to become negative and even diverge at some particular working points.

2.4 The Josephson bifurcation amplifier

(Palacios-Laloy, 2010)

$$[L_e + L_J(i)]\ddot{q} + R_e \dot{q} + \frac{q}{C_e} = V_e \cos(\omega_m t) \tag{2.9}$$

Expanding this to second order in L_J leads to the expression

$$\left(L_e + L_J \left[1 + \frac{\dot{q}^2}{2I_0^2}\right]\right)\ddot{q} + R_e \dot{q} + \frac{q}{C_e} = V_e \cos(\omega_m t) \tag{2.10}$$

Defining the total inductance $L_t = L_e + L_J$, the participation ratio $p = L_J/L_t$, the resonance frequency $\omega_r = 1/\sqrt{L_t C_e}$ and the quality factor $Q = \omega_r L_t / R_e$ we can rewrite this as

$$\ddot{q} + \frac{\omega_r}{Q}\dot{q} + \omega_r^2 q + \frac{p\dot{q}^2\ddot{q}}{2I_0} = \frac{V_e}{L_t} \cos(\omega_m t) \tag{2.11}$$

Chapter 3

Realizing a Two-Qubit Processor

This chapter discusses the main experimental results of this thesis. We start by discussing the implementation of a superconducting two-qubit processor, discussing the characteristics of the Transmon qubits used in the processor, the readout scheme, single-qubit manipulation, two-qubit gates as well as the experimental procedures used for quantum state and quantum process tomography. The last section of this chapter will discuss the implementation of a quantum algorithm – so called Grover search algorithm – using our two-qubit processor and the demonstration of quantum speed-up achieved with our system.

3.1 Introduction & Motivation

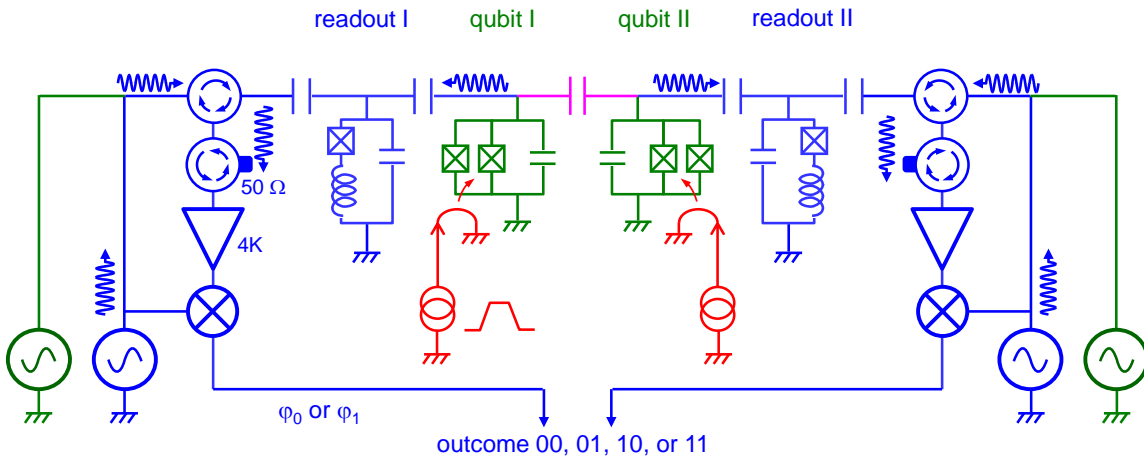Figure 3.1: The circuit schematic of the two-qubit processor used in this work. Shown are the two Transmon qubits in green, the drive and readout circuit in blue, the fast flux lines in red and the coupling capacitance in magenta.

As discussed in the introduction, the most simple, usable quantum processor contains two qubits that are coupled by an universal two-qubit gate and which in addition

can be manipulated and read out individually. We realized such a two-qubit processor using two Transmon qubits, coupled through a fixed capacitance and readout out by individual single-shot readout of the JBA type. The circuit diagram of our processor is shown in fig. 3.1, showing the qubits, the drive and readout circuit and the coupling element between them. The following sections we'll discuss the parameters of individual parts of the processor.

3.2   Processor Design

The parameters of the sample have been chosen in accordance to various design constraints of the qubit processor. For the qubits, the main design goals were high coherence time, good frequency tunability and fast drivability. As we will show later, the coherence time of the qubit is limited by relaxation to the ground state and coupling to external noise sources. The relaxation component of the Transmon qubit is ultimately limited by internal losses of the Josephson junction but usually is bound by coupling to the electromagnetic environment, as will be discussed later. The frequency tunability is important for the realization of fast two-qubit gates but can also limit the relaxation and coherence time of the qubit by coupling to external noise sources. The drivability speed on the other hand is limited by the anharmonicity of the qubit, which can however not be increased arbitrarily since it will make the qubit sensitive to charge noise when chosen too high. For the readout, the main design goals were readout speed and fidelity. The speed of the readout is limited by the quality factor of the readout resonator, which however also can induce qubit relaxation through the Purcell effect and may therefore not be chosen too small.

In the following paragraphs we'll therefore discuss the parameter design for our two-qubit processor and analyze the sample parameters that have been obtained.

3.3   Processor Fabrication

In this section we will discuss the fabrication of the two-qubit processor realized in this work.

Chapter 4

Measurement Setup

Fig. 4.1 show the measurement setup used for the two-qubit experiments. The different signal and measurement lines as well as the room-temperature and cryogenic microwave components used in our experiments will be described in the following paragraphs.

In this section we discuss the details of the measurement setup used to perform the two-qubit experiments presented in this thesis. All experiments have been performed in a custum-built dilution cryostat at $< 40 \text{ mK}$ using a cryogenic microwave signal generation and measurement chain. The individual components of this setup will be discussed in the following sections.

4.1 Sample Holder & PCB

The qubit chip is first glued to a high-frequency PCB !9! , then wirebonds are used to connect the groundplane and the center conductors of the on-chip transmission lines to their counterparts on the PCB. Finally, additional bond wires connect isolated ground planes on-chip. The realization of a good and uniform groundplane on the qubit chip and around is very important to supress unwanted resonance modes that can be created when the connection between isolated ground planes is not good enough !10! . The mounted chip on the PCB is then placed in a Copper or Aluminium sample holder which fully encloses the PCB and serves to reduce unwanted couplings to the environment. The coplanar waveguides on the PCB are connected to Mini-SMP cables through a set of connectors that are soldered on the PCB.

To Do 9: add substrate material details

To Do 10: Add references e.g. to Schuster's thesis
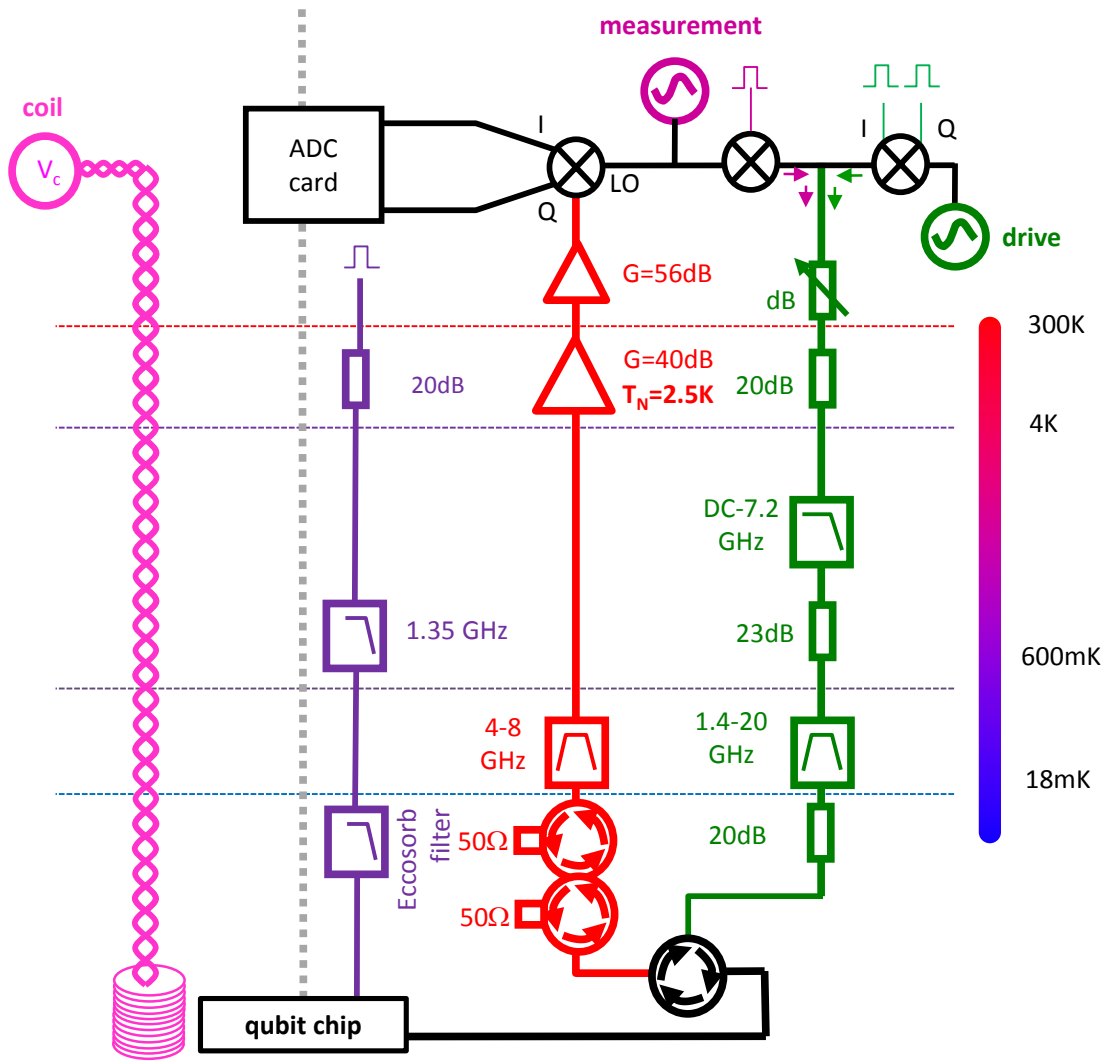
Figure 4.1: The measurement setup used for the two-qubit experiments. Exactly the same drive and readout scheme is used for both qubits with phase-locked microwave sources and arbitrary waveform generators.

4.2   Cryogenic wiring

For the transmission of microwave signals to our sample we use various types of transmission lines suited for room-temperature and cryogenic application. The main goal of the input lines is to provide adequate signal transmission without introducing too much thermal conductance to the system. For the signal lines that carry the measurement signal from the sample we use superconducting cables !11! and low-resistance copper cables. In addition, we use superconducting bifilar cables for the DC bias of our magnetic coils. The qubit and fluxline input lines are attenuated and filtered at several stages of the cryostat to reduce signal noise.

To Do 11: add type

4.3 Signal Generation & Acquisition

Here we discuss the generation and acquisition of the different signals used to manipulate and read out our quantum processor. The experiments that have been performed require the generation, measurement and demodulation of microwave signals, the generation of fast flux control pulses and the application of DC currents to our magnetic coils.

4.3.1 Microwave sideband mixing

For qubit manipulation it is often advantageous to use single-sideband mixing for driving the qubit since it can provide higher ON/OFF ratios for microwave pulses and allow the driving of higher qubit-levels using a single, phase-coherent microwave source. To realize this, we use IQ mixers (Hittite !12!) that we drive with a continous single-frequency microwave tone and two time-synchronized fast control signals generated by an arbitrary waveform generator (Tektronix AWG5014b). When feeding a signal $LO(t) = i_0 \cos(\omega_{rf} t)$ to the LO port of the mixer and two signals $I(t)$, $Q(t)$ to the I and Q ports of the mixer one obtains a signal

To Do 12: Add exact type number

$$RF(t) = I(t) \cos(\omega_{rf} t) + Q(t) \sin(\omega_{rf} t) \tag{4.1}$$

at the LO port of the mixer. Since the IQ mixer that we use is a passive, reciprocal device one can as well feed two input signals to the LO and RF ports and obtain the demodulated signal quadratures at the I and Q ports, a technique that we'll make use of for our qubit readout scheme.

Commercially available IQ mixers often deviate from the ideal behavior as given by eq. (4.1). Typical imperfections include large insertion losses –i.e. loss of signal power between the different ports of the mixer–, RF signal leakage at zero IQ-input and frequency-dependent phase and amplitude errors of the mixed sideband signals. In order to achieve reliable single-qubit operations we need to correct the signal leakage and quadrature-specific amplitude and phase errors. The signal leakage causes a small part of the LO signal to leak through to the RF port even when the IQ inputs are zeroed. This leakage can be compensated by adding center-frequency ω_c dependent DC offset voltages to the IQ ports. The appropriate offset voltages can be determined by applying a continuous input signal at a frequency ω_c to the LO port of the mixer and minimizing the signal power at the RF port by varying the IQ offset voltages. To correct the sideband amplitude and phase errors we apply another correction procedure that we outline here. First, for the signals at the IQ inputs of the mixer we introduce the notation

$$A(t) = I(t) + iQ(t) = a(t) \exp(-i\phi(t)) \tag{4.2}$$

We consider an IQ signal at a single sideband frequency ω_{sb} and at fixed complex amplitude $a(t) = a = a_0 \exp(i\phi_0)$ such that $A(t) = a \exp(-i\omega_{sb}t)$. The effect of the gain and phase imperfections of the IQ mixers can then be modeled by assuming that the mixer adds another IQ signal $\epsilon(\omega_{sb}, \omega_c)A^*(t)$ at the mirrored sideband frequency $-\omega_{sb}$. We can correct this unwanted signal by adding a small correction $c(\omega_{sb}, \omega_c)A^*(t)$ to our IQ input signal. The correction coefficient $c(\omega_{sb}, \omega_c)$ usually depends both on the carrier frequency ω_c and the sideband frequency ω_{sb}. We determine the correction coefficients by generating a continuous waveform at a given center and sideband frequency, measuring the amplitude of the unwanted sideband signal with a fast spectrum analyzer and minimizing its amplitude by varying the correction coefficient $c(\omega_s b, \omega_c)$.

Both the offset and the sideband-amplitude and -phase corrections have been automatized using our data acquisition software, the resulting correction coefficients are summarized in fig. **??**.

4.3.2 Fast magnetic flux pulses

The fast flux lines are implemented by a pair of superconducting 50 Ω transmission lines, which are attenuated by 20 dB and filtered at the 4K and 20 mK stages of the cryostat. The filtering at the 20 mK stage is realized through custom-made, highly absorptive Eccosorb filters. Fig. **??** shows an image of these filters and the attenuation characteristic obtained. The heavy filtering of the flux line greatly reduces noise seen by the qubit but also distorts all signals sent through the line. This distortion is unwanted especially at high frequencies and needs to be corrected. To do this we need to

Figure 4.2: (response function filtered with a Gaussian filter with a cut-off at 0.4 GHz)

measure and compensate the frequency response of the flux line at experimental conditions. In order to do this, we feed back the flux signal sent to the sample through a transmission line which is exactly equivalent to the input line. This allows us to measure the returning signal at room temperature and – assuming symmetric distortion in the in-

put and return line – to calculate the response function of the input line. Fig. 4.2 shows the different parts of the response function of the flux line as measured in our experiment. After eliminating the response of the analog-to-digital converter we can calculate the response function between the input port of the flux line and the sample by solving the equation

$$... \tag{4.3}$$

4.3.3 Pulse synchronization

Chapter 5

Measurement techniques

In this section we will discuss the techniques used to characterize and manipulate our two-qubit processor. All techniques employed are based on ...

5.1   Saturation spectroscopy

5.2   Rabi oscillations

5.3   Measuring relaxation time

5.4   Measuring dephasing time

Chapter 6

Processor Characterization

This section discusses the detailed characterization of individual circuit parts that will be used later to realize two-qubit gate and to run a quantum algorithm on the processor. The discussion will focus on the readout and microwave manipulation of the qubits as well as on the reconstruction of quantum states from measurement data, which will be used later for characterizing gate and processor operation.

6.1   Spectroscopic measurements

The following section discusses the parameters of our two-qubit processor that have been obtained by various measurements.

6.1.1   Qubit Parameters

6.1.2   Readout Parameters

- *Qubits*: Spectroscopic measurement of the qubit transitions yielded parameter values of $E_J^I/h = 36.2$ GHz, $E_c^I/h = 0.98$ GHz and $E_J^{II}/h = 43.1$ GHz, $E_C^{II}/h = 0.87$ GHz for the Josephson and charging energies of the two qubits and values of $d^I = 0.2$, $d^{II} = 0.35$ for the qubit junction asymmetries.

- *Readout resonator*: The frequencies of the readout resonators have been measured as $\nu_R^I = 6.84$ GHz and $\nu_R^{II} = 6.70$ GHz with quality factors $Q^I \simeq Q^{II} = 730$, independent measurements of the Kerr nonlinearities yielded $K^I/\nu_R^I \simeq K^{II}/\nu_R^{II} = -2.3 \pm 0.5 \times 10^{-5}$!13! .

- *Qubit-Resonator coupling*: The coupling of the qubits to the readout resonators has been spectroscopically determined as $g_0^I \simeq g_0^{II} = 50$ MHz
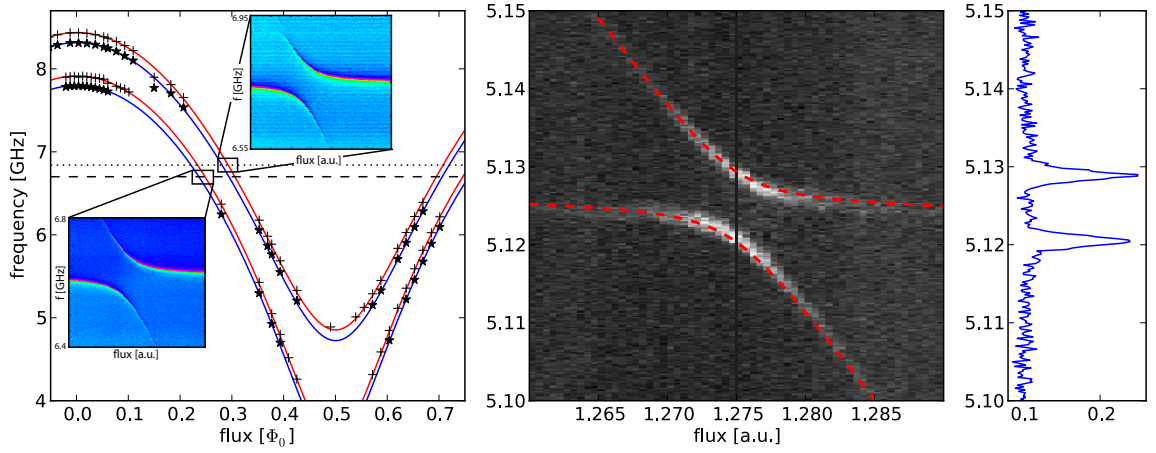
Figure 6.1: Spectroscopy of the realized two-qubit processor. a) $|0\rangle \rightarrow |1\rangle$ and $(|0\rangle \rightarrow |2\rangle)/2$ transition frequencies of the two qubits with fitted dependence and cavity frequencies. b) Avoided level crossing of the $|01\rangle$ and $|10\rangle$ levels of the qubits with fit, $g = 8.7$ MHz. c) Spectroscopy of qubit 1 at the point indicated in b).

Figure 6.2

6.2   Readout Characterization

6.3   Single-Qubit Operations

6.4   Quantum State Tomography

Quantum state tomography is the procedure of experimentally determining an unknown quantum state(Michael A. Nielsen and Isaac L. Chuang, 2000).

Figure 6.3

The density matrix of an n-qubit system can be written in general form as

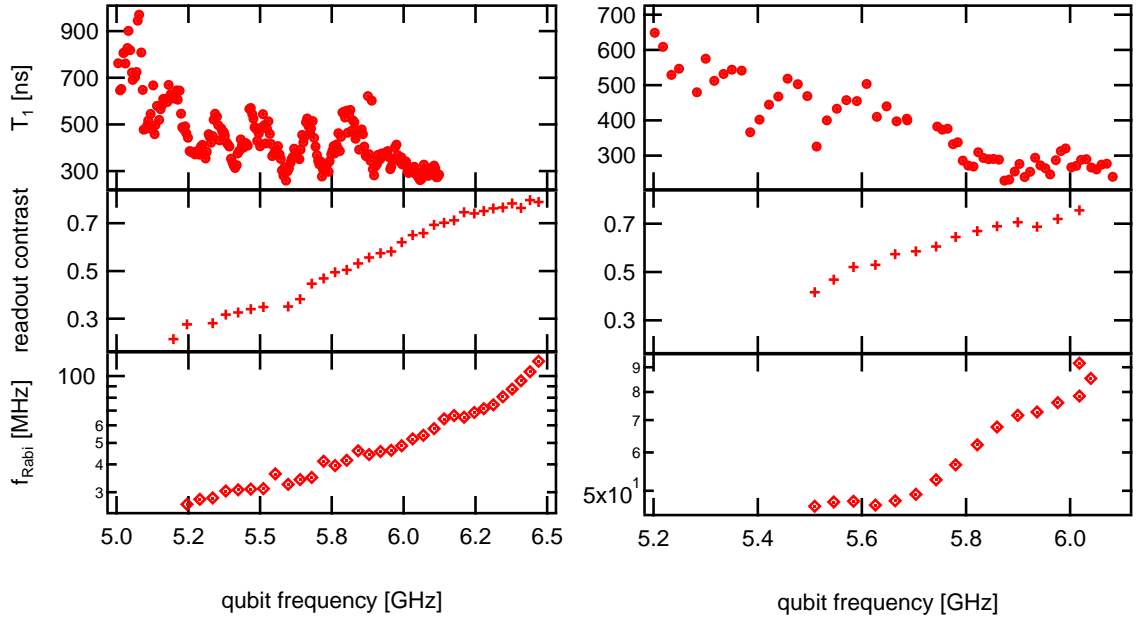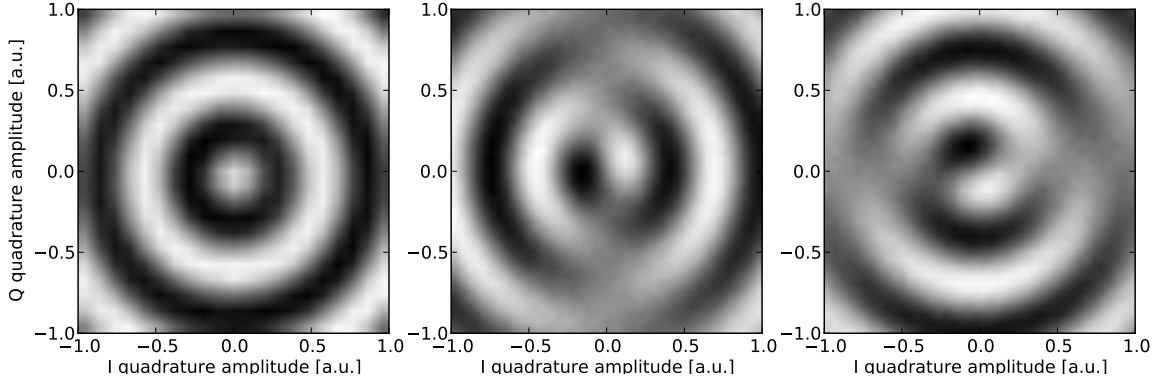$$\rho = \sum_{v_1,v_2...v_n} \frac{c_{v_1,v_2...v_n}\sigma_{v_1} \otimes \sigma_{v_2}...\sigma_{v_n}}{2^n} \tag{6.1}$$

$$c_{v_1,v_2...v_n} = \text{tr}\left(\sigma_{v_1} \otimes \sigma_{v_2}...\otimes \sigma_{v_n}\,\rho\right) \tag{6.2}$$

where $v_i \in \{X, Y, Z, I\}$ and n gives the number of qubits in the system and where the $c_{v_1,v_2...v_n}$ are real-valued coefficients that fully describe the given density matrix. To reconstruct the density matrix of an experimental quantum system in a well-prepared state it is therefore sufficient to measure the expectation values of these $n^2 - 1$ coefficients on an ensemble of identically prepared systems. However, statistical and systematic measurement errors can yield a set of coefficients that corresponds to a *non-physical* density matrix which violates either the positivity or unity-trace requirement. In the following paragraph we will therefore discuss a technique with which one can estimate the density matrix of a system in a more correct way.

6.4.1 Maximum Likelihood Estimation

A method which is often used in quantum state tomography is the so-called *maximum-likelihood* technique. Rather than directly calculating the density matrix of the system from the obtained expectation values $c_{v_1,v_2...v_n}$, it calculates the joint probability of measuring a set $\{c_{X,X,...,X}, c_{Y,X,...,X}, ..., c_{I,I,...,I}\}$ for a given estimate of the density matrix $\hat{\rho}$. By numerically or analytically maximizing this joint probability over the set of possible density matrices we obtain the density matrix which is most likely to have produced the set of measurement outcomes that we have observed.

The joint measurement operators $\Sigma_j = \sigma_{v_1} \otimes \sigma_{v_2}...\otimes \sigma_{v_n}$ have the eigenvalues ± 1

and can thus be written as

$$\sigma_{v_1} \otimes \sigma_{v_2} \ldots \otimes \sigma_{v_n} = |{+}_j\rangle \langle {+}_j| - |{-}_j\rangle \langle {-}_j| \tag{6.3}$$

where $|{-}_j\rangle$ and $|{-}_j\rangle$ are the eigenstates corresponding to the eigenvalues ± 1 of Σ_j. The expectation value $\langle \Sigma_j \rangle$ can be estimated by the quantity

$$\widehat{\langle \Sigma_j \rangle}_\rho = \frac{1}{l} \sum_{i=1}^{l} M_i(\Sigma_j, \rho) \tag{6.4}$$

where $M_i(M, \rho)$ denotes the outcome of the i-th measurement of the operator M on the state described by the density matrix ρ. This quantity is binomially distributed with the expectation value $E(\widehat{\langle \Sigma_j \rangle}_\rho) = \langle \Sigma_j \rangle_\rho$ and the variance $\sigma^2(\widehat{\langle \Sigma_j \rangle}_\rho) = 1/l \cdot (1 - \langle \Sigma_j \rangle_\rho^2)$. For large sample sizes l, the binomial distribution can be well approximated by a normal distribution with the same expectation value and variance. The joint probability of obtaining a set of measurement values $\{s_1, \ldots, s_{n^2-1}\}$ for the set of operators $\{\widehat{\langle \Sigma_1 \rangle}_\rho, \ldots, \widehat{\langle \Sigma_{n^2-1} \rangle}_\rho\}$ is then given as

$$P\left(\widehat{\langle \Sigma_1 \rangle}_\rho = s_1; \ldots; \widehat{\langle \Sigma_{n^2-1} \rangle}_\rho = s_{n^2-1}\right) = \prod_{i=1}^{n^2-1} \exp\left(-\frac{l}{2} \frac{(s_i - \langle \Sigma_i \rangle_\rho)^2}{1 - \langle \Sigma_i \rangle_\rho^2}\right) \tag{6.5}$$

By maximizing this probability (or the logarithm of it) we obtain an estimate of the density matrix ρ of the quantum state. This technique also allows us to include further optimization parameters when calculating the joint probability. This is useful for modeling e.g. systematic errors of the measurement or preparation process, which can be described by modifying the operators contained in the probability sum. A common source of errors in our tomography measurements are errors in the microwave pulses used to drive the qubit. Since our measurement apparatus permits us only to measure the σ_z operator of each qubit we have to perform $\pi/2$ rotations about the Y or $-X$ axes of the Bloch sphere of each individual qubit in order to measure the values of the σ_x and σ_y operators, which we therefore replace with an effective measurement of each qubits σ_z operator preceded by a rotation R_{ν_i} given as

$$R_X = \exp\left(-i\sigma_y \pi/4\right) \tag{6.6}$$
$$R_Y = \exp\left(+i\sigma_x \pi/4\right) \tag{6.7}$$

Phase and amplitude errors can be modeled as

$$R_X = \exp\left(-i\left[+\sigma_y \cos\alpha + \sigma_x \sin\alpha\right]\left[\pi/4 + \gamma\right]\right) \tag{6.8}$$
$$R_Y = \exp\left(+i\left[-\sigma_y \sin\beta + \sigma_x \cos\beta\right]\left[\pi/4 + \delta\right]\right) \tag{6.9}$$
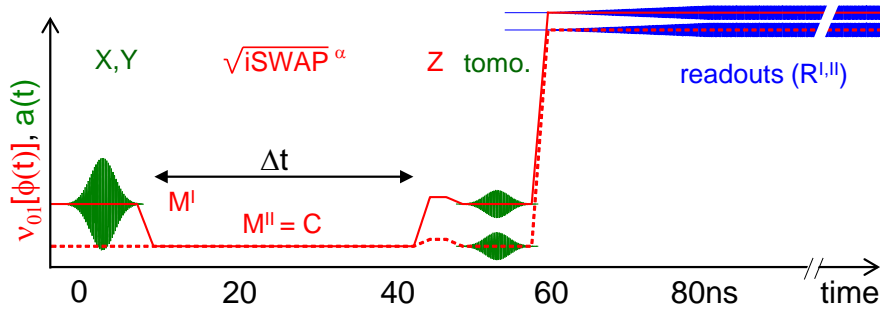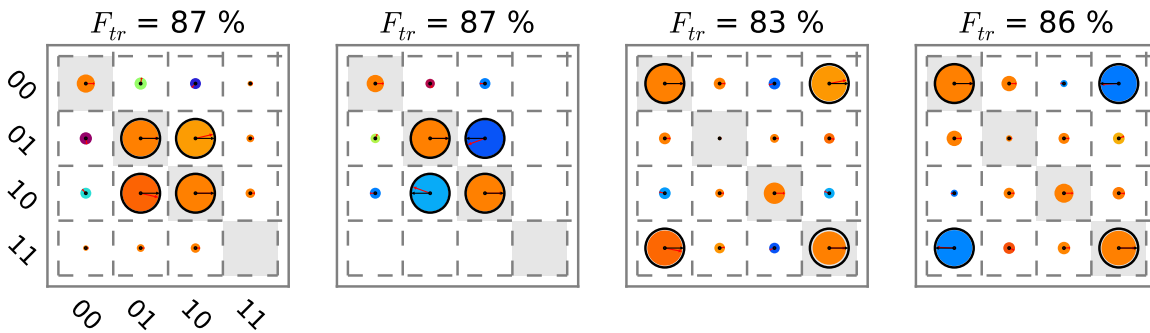
Figure 6.4

Figure 6.5: Experimentially created $|\psi_+\rangle$ ($F = 0.91$) and $|\psi_-\rangle$ ($F = 0.93$) states

Here, α and β represent phase errors whereas γ and δ represent amplitude errors in the drive pulses.

6.5 Two Qubit Operations

6.5.1 Creation of Entanglement

6.5.2 Violation of Bell's inequality

6.6 Quantum Process Tomography

6.6.1 Introduction & Principle

6.6.2 Implementation

A quantum process can be described as a map $\mathcal{E} : \rho_{\mathcal{H}} \rightarrow \rho_{\mathcal{H}}$ that maps a density matrix ρ defined in a Hilbert space Q_1 to another density matrix $\mathcal{E}(\rho)$ defined in a target Hilbert space Q_2 and fulfilling three axiomatic properties Michael A. Nielsen and Isaac L. Chuang (2000); Haroche and Raimond (2006):
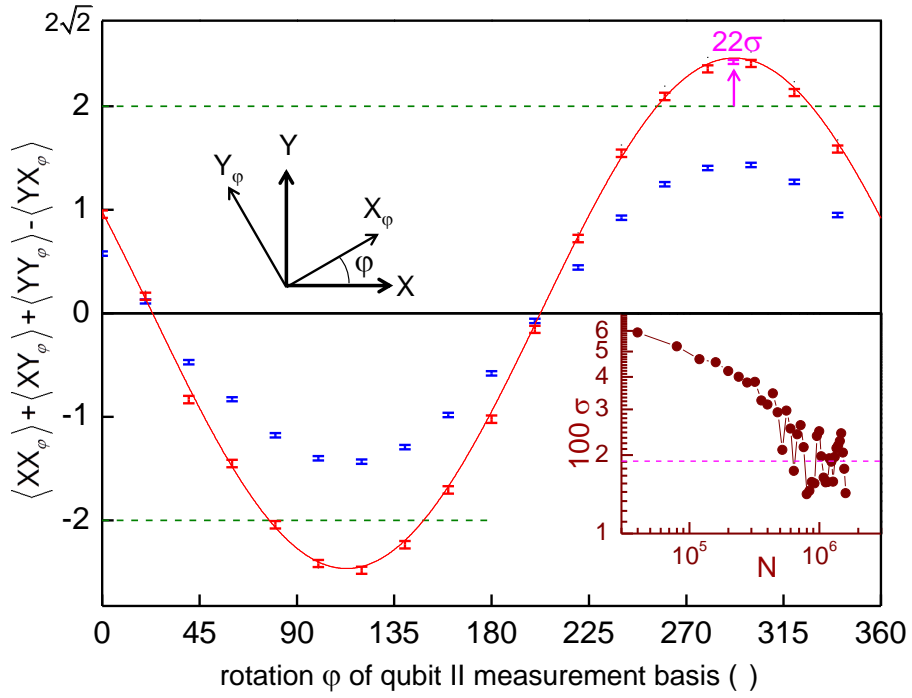
Figure 6.6

Axiom 6.0.1. $\mathrm{tr}\left[\mathcal{E}(\rho)\right]$ is the probability that the process represented by $\mathcal{E}$ occurs, when ρ is the initial state.

Axiom 6.0.2. $\mathcal{E}$ is a *convex-linear map* on the set of density matrices, that is, for probabilities $\{p_i\}$,

$$\mathcal{E}\left(\sum_i p_i \rho_i\right) = \sum_i p_i \mathcal{E}(\rho_i) \tag{6.10}$$

Axiom 6.0.3. $\mathcal{E}$ is a *completely-positive* map. That is, if $\mathcal{E}$ maps density operators of system Q_1 to density operators of system Q_2, then $\mathcal{E}(A)$ must be positive for any positive operator A. Furthermore, if we introduce an extra system R of arbitrary dimensionality, it must be true that $(\mathcal{I} \otimes \mathcal{E})(A)$ is positive for any positive operator A on the combined system RQ_1, where $\mathcal{I}$ denotes the identity map on system R.

As shown in Michael A. Nielsen and Isaac L. Chuang (2000), any quantum process fulfilling these criteria can be written in the form

$$\mathcal{E}(\rho) = \sum_i E_i \rho E_i^\dagger \tag{6.11}$$

for some set of operators $\{E_i\}$ which map the input Hilbert space to the output Hilbert space, and $\sum_i E_i^\dagger E_i \leq I$.

Now, if we express the operators E_i in a different operator basis $\tilde{E}_j$ such that $E_i = \sum_j a_{ij} \tilde{E}_j$ and insert into eq. (6.11), we obtain

$$\mathcal{E}(\rho) \;=\; \sum_i \sum_j a_{ij} \tilde{E}_j \, \rho \, \sum_k a_{ik}^* \tilde{E}_k^\dagger \tag{6.12}$$

$$=\; \sum_{j,k} \tilde{E}_j \, \rho \, \tilde{E}_k^\dagger \sum_i a_{ij} a_{ik}^* \tag{6.13}$$

$$=\; \sum_{j,k} \tilde{E}_j \, \rho \, \tilde{E}_k^\dagger \, \chi_{jk} \tag{6.14}$$

where we defined $\chi_{jk} = \sum_i a_{ij} a_{ik}^*$. This is the so-called χ-matrix representation of the quantum process. Here, all the information on the process is contained in the χ matrix, which controls the action of the process-independent operators $\tilde{E}_i$ on the initial density matrix ρ.

Now, the goal of *quantum process tomography* is to obtain the coefficients of the χ-matrix – or any other complete representation of the process – from a set of experimentally measured density matrices ρ and $\mathcal{E}(\rho)$.

To achieve this, several techniques have been developed. The technique used in this work is the so-called *standard quantum process tomography (SQPT)*. This technique proceeds as follows:

1. Choose a set of operators E_i that forms a full basis of $\mathcal{M} : Q_1 \to Q_2$. For n-qubit process tomography we usually choose $E_{i_1,i_2\ldots i_n} = \sigma_{i_1} \otimes \sigma_{i_2} \ldots \otimes \sigma_{i_n}$, where σ_i are the single-qubit Pauli operators and $i \in \{I, X, Y, Z\}$.

2. Choose a set of pure quantum states $|\phi_i\rangle$ such that $|\phi_i\rangle \langle\phi_i|$ span the whole space of input density matrices ρ. Usually, for a n-qubit system we choose $\phi = \{|0\rangle, |1\rangle, (|0\rangle + |1\rangle)/\sqrt{2}, (|0\rangle + i|1\rangle)/\sqrt{2}\}^{\otimes n}$, where $^{\otimes n}$ denotes the n-dimensional Kronecker product of all possible permutations.

3. For each of the $|\phi_i\rangle$, determine $\mathcal{E}(|\phi_i\rangle \langle\phi_i|)$ by quantum state tomography. Usually we also determine $|\phi_i\rangle \langle\phi_i|$ experimentally since the preparation of this state already entails small preparation errors that should be taken into account when performing quantum process tomography.

After having obtained the ρ_i and $\mathcal{E}(\rho_i)$ one obtains the χ-matrix by writing $\mathcal{E}(\rho_i) = \sum_j \lambda_{ij} \tilde{\rho}_j$, with some arbitrary basis $\tilde{\rho}_j$ and letting $\tilde{E}_m \tilde{\rho}_j \tilde{E}_n^\dagger = \sum_k \beta_{jk}^{mn} \tilde{\rho}_k$. We can then insert into eq. (6.14) and obtain

$$\sum_k \lambda_{ik} \tilde{\rho}_k \;=\; \sum_{m,n} \chi_{mn} \sum_k \beta_{ik}^{mn} \tilde{\rho}_k \tag{6.15}$$

This directly yields $\lambda_{ik} = \sum_{m,n} \beta_{ik}^{mn} \chi_{mn}$, which, by linear inversion, gives χ.

6.6.3   The Kraus representation

Besides the χ-matrix representation, there is another useful way of expressing a quantum map, the so called *Kraus representation*, which is given as

$$\mathcal{E}(\rho) = \sum_i M_i \, \rho \, M_i^\dagger \tag{6.16}$$

It can be shown (Haroche and Raimond, 2006) that this sum contains at most N elements, where N is the dimension of the Hilbert space of the density matrix ρ. We can go from the χ representation to the Kraus representation by changing the basis $\tilde{E}_i$ such that

$$\tilde{E}_i = \sum_l a_{il} \, \breve{E}_l \tag{6.17}$$

which, for eq. (6.14), yields

$$\begin{aligned}
\mathcal{E}(\rho) &= \sum_{j,k} \sum_l a_{jl} \breve{E}_l \, \rho \sum_m a_{km}^* \breve{E}_m^\dagger \, \chi_{jk} \tag{6.18} \\
&= \sum_{l,m} \breve{E}_l \, \rho \, \breve{E}_m^\dagger \sum_{j,k} a_{jl} a_{km}^* \chi_{jk} \tag{6.19}
\end{aligned}$$

The last sum on the right side of eq. (6.19) corresponds to a change of coordinates of the matrix χ. Now, we can pick the a such that χ is diagonal in the new basis $\breve{E}$ and obtain

$$\begin{aligned}
\mathcal{E}(\rho) &= \sum_l \lambda_l \breve{E}_l \, \rho \, \breve{E}_l^\dagger \tag{6.20} \\
&= \sum_l M_l \, \rho \, M_l^\dagger \tag{6.21}
\end{aligned}$$

with λ_l being the l-th eigenvalue of the χ matrix with the eigen-operator $\breve{E}_l$ and $M_l = \sqrt{\lambda_l} \breve{E}_l$.
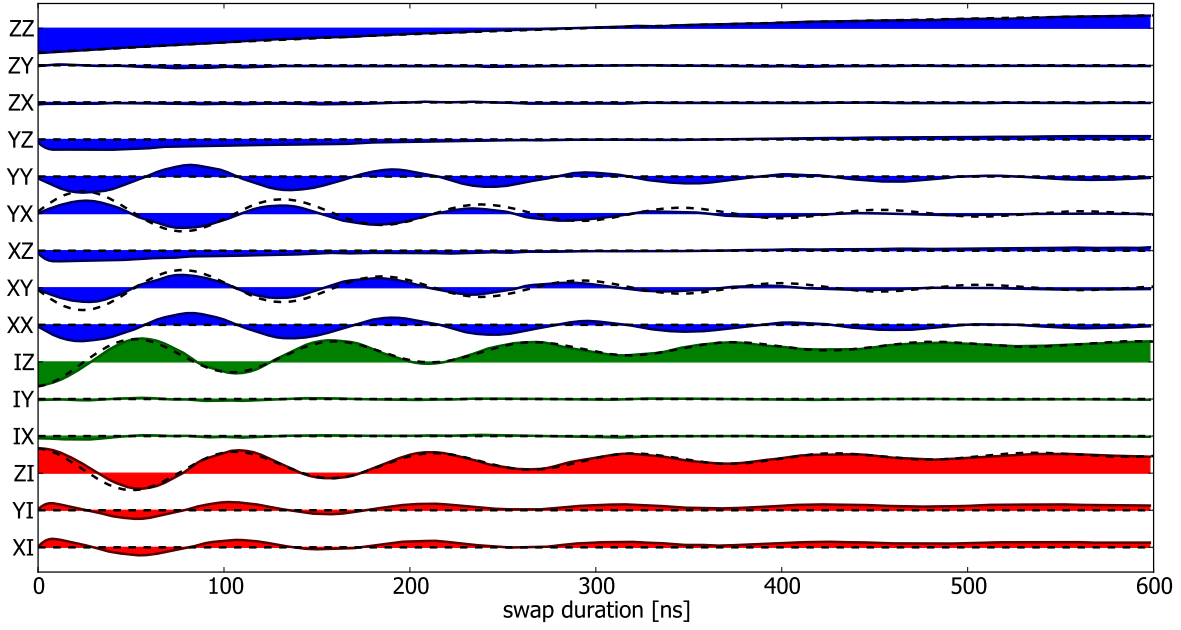
Figure 6.7: Measured Pauli operators $\sigma_i \otimes \sigma_j$ with $i, j \in \{X, Y, Z, I\}$ as a function of the interaction time. Shown are the 6 single-qubit operators as well as the 9 two-qubit correlation operators. The dashed line represents a master-equation simulation of the experiment.

6.7 Realizing a Two-Qubit Gate

6.7.1 Principle

6.7.2 Implementation

6.7.3 Fidelity

6.7.4 Error Analysis

Figure 6.8: The input-output density matrix of the quantum process tomography of the $\sqrt{i\overline{\text{SWAP}}}$ gate. Shown are the measured density matrices of 16 different input states and the corresponding output matrices with their state fidelities. The ideal matrices are overlaid in red.
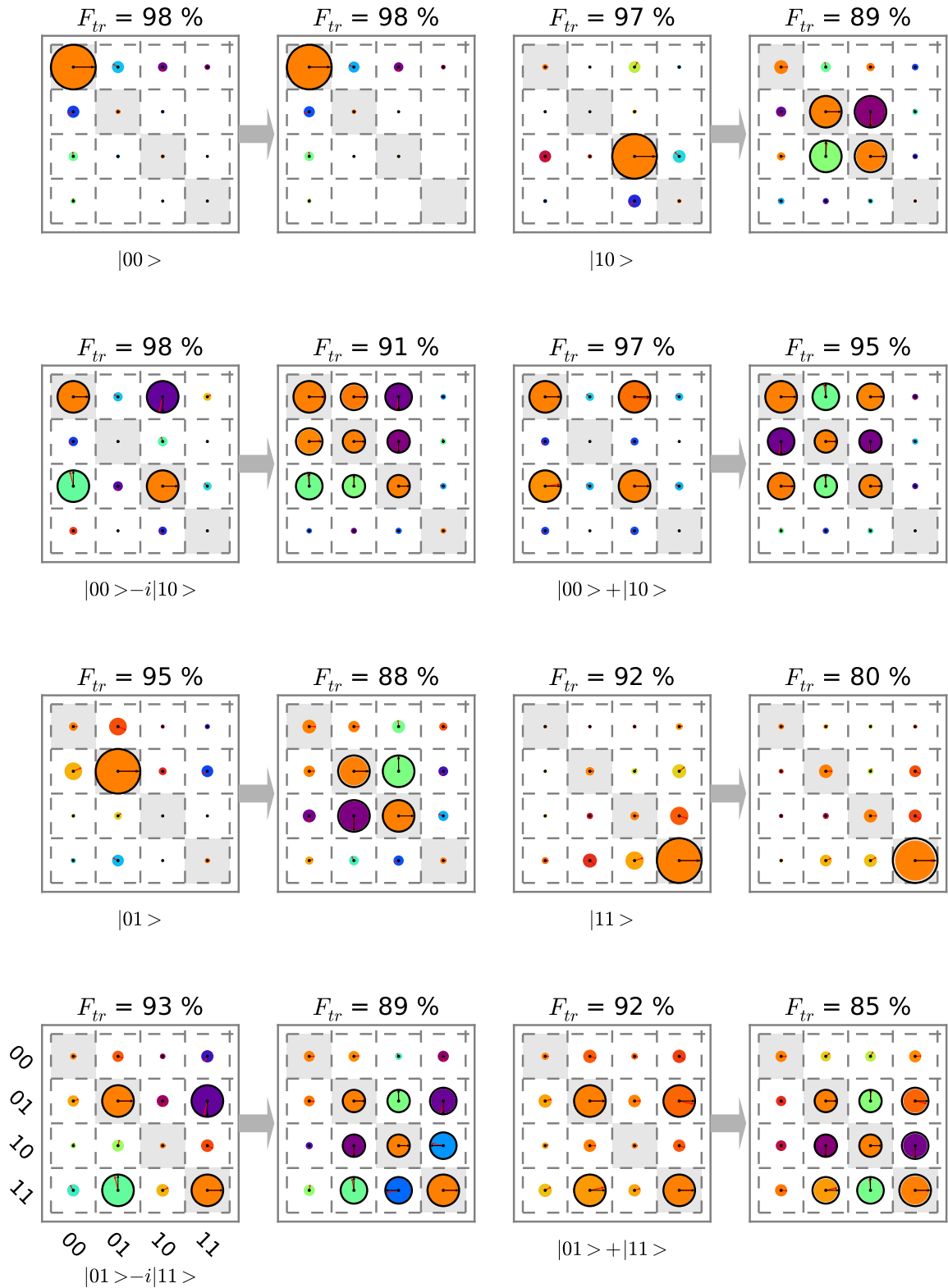
Figure 6.9: The input-output density matrix of the quantum process tomography of the $\sqrt{i\text{SWAP}}$ gate. Shown are the measured density matrices of 16 different input states and the corresponding output matrices with their state fidelities. The ideal matrices are overlaid in red.
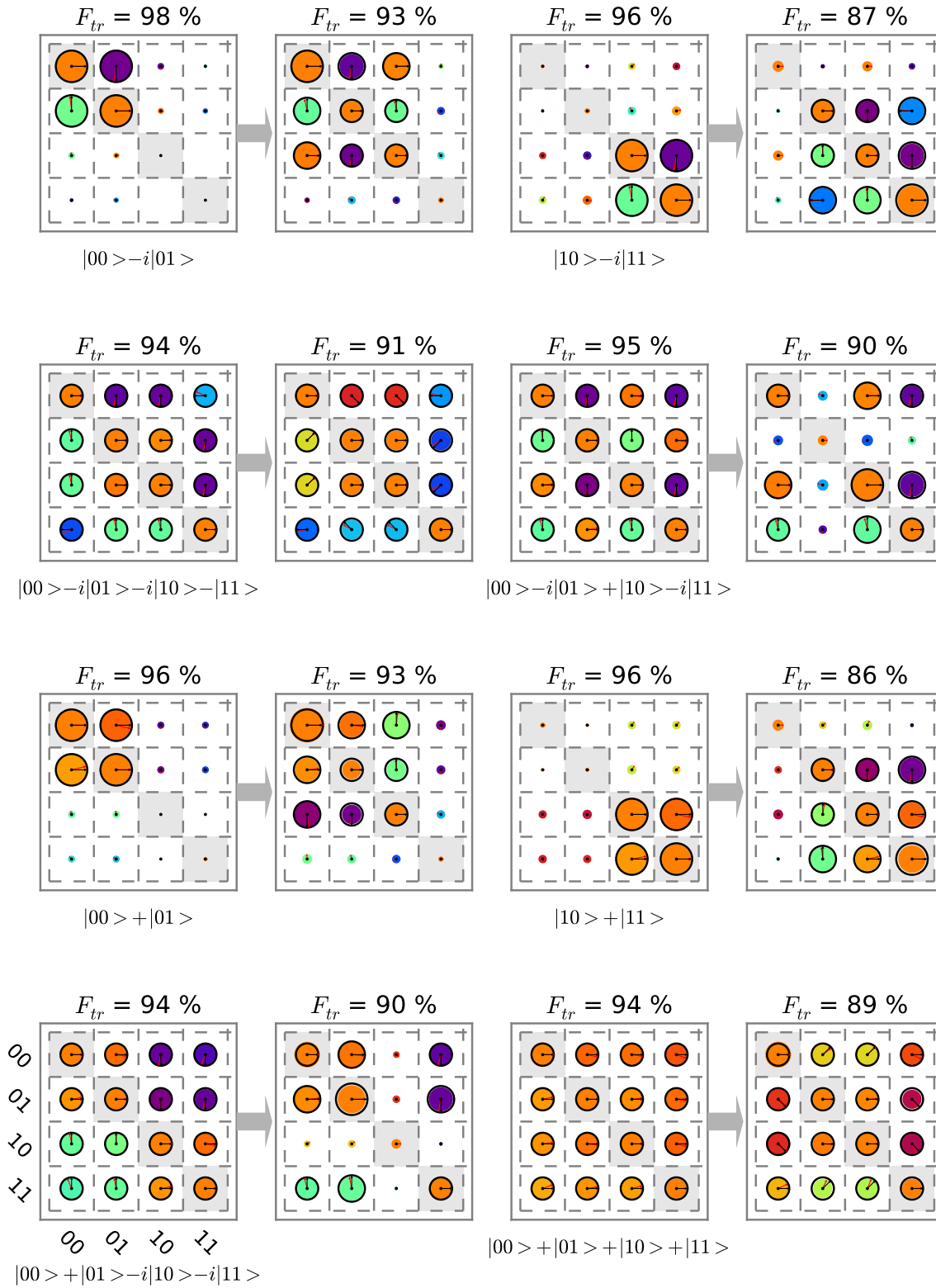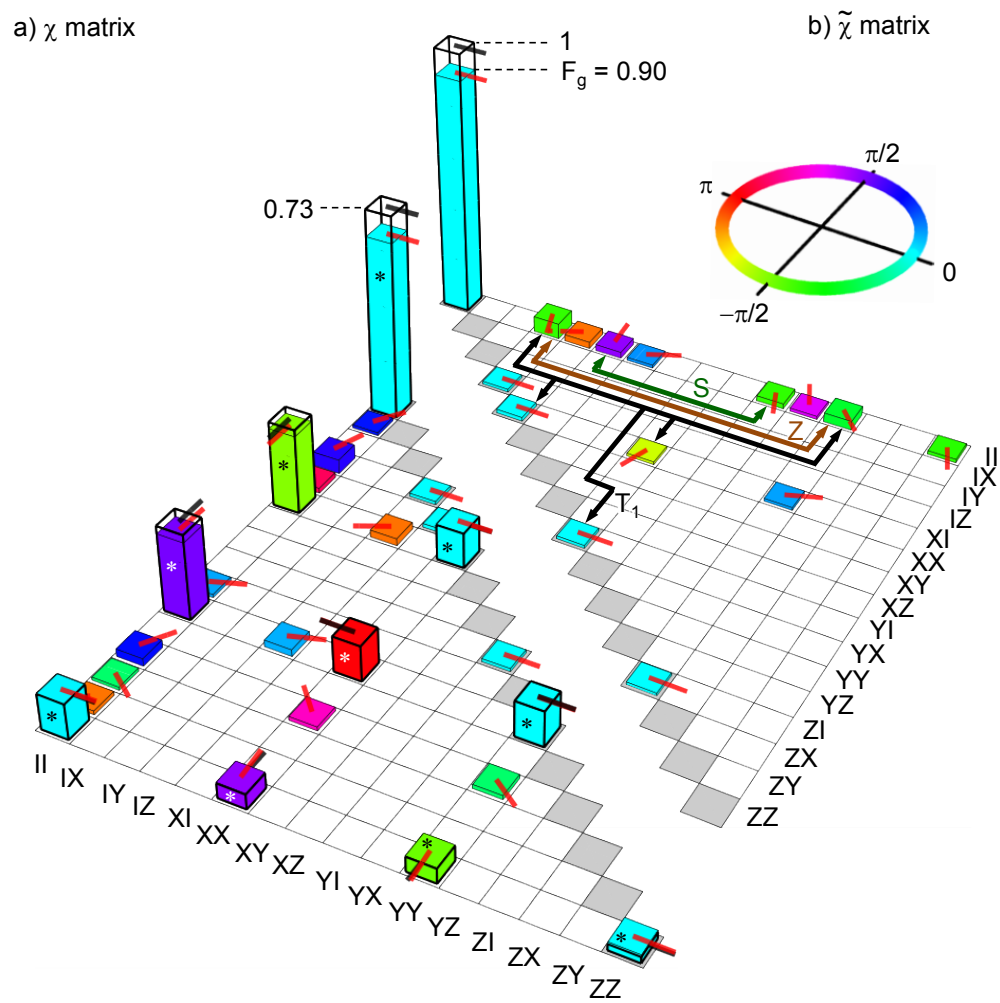
a) χ matrix

b) $\tilde{\chi}$ matrix

Figure 6.10

Chapter 7

Running the Grover Search Algorithm

7.1 Introduction & Motivation

The original algorithm by as given by Grover (1997) is given as follows

1. Start with the qubit register in the state $|\psi\rangle = |000\ldots0\rangle$

2. Apply the Hadamard operation to the qubit register, producing the equally superposed state

$$|\psi\rangle = \frac{1}{\sqrt{n}} \sum_i^n |i\rangle$$

.

3. Repeat the following sequence $\mathcal{O}(\sqrt{n})$ times:

    Apply the oracle operator $|i\rangle \rightarrow (-1)^{\delta_i^j} |i\rangle$ to the state $|\psi\rangle$, where $|j\rangle$ is the state marked by the oracle.

    Apply the diffusion operator $|i\rangle \rightarrow -|i\rangle + \frac{2}{n} \sum_i^n |j\rangle$ to the state $|\psi\rangle$.

4. Measure the state of the quantum register

The seemingly elusive algorithm can be derived in a very clear way from Schrödinger's equation, as shown in the seminal paper by Grover (2001). Since the derivation given in this paper sheds some interesting light on the nature of the quantum search algorithm we will discuss it here. The derivation begins by considering a quantum system governed by Schrödinger's equation, which can be written as (omitting all physical constants for the sake of clarity)

$$-i\frac{\delta}{\delta t}\psi(x,t) = \frac{\delta^2}{\delta x^2}\psi(x,t) - V(x)\psi(x,t) \tag{7.1}$$

Here $\psi(x,t)$ describes the wave-function and V is a time-indepenent potential. Let us assume that the potential $V(x)$ is shaped as in fig. **??**a, i.e. possessing a local
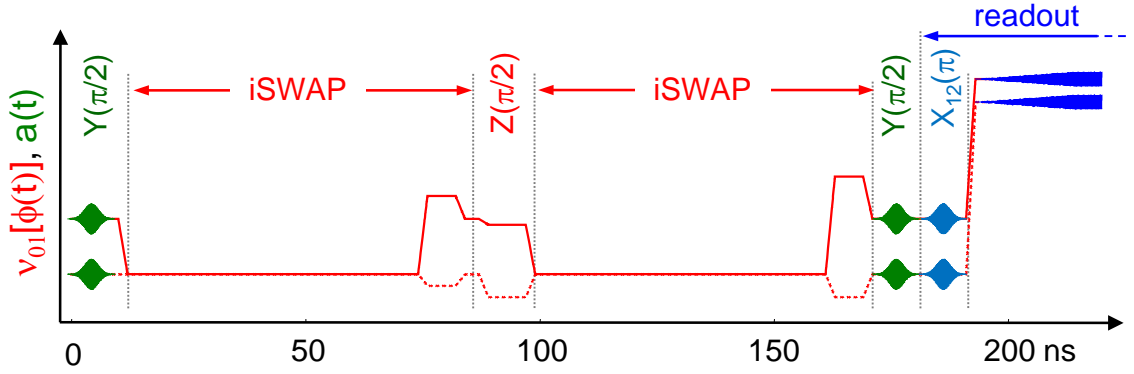
Figure 7.1: The pulse sequence used in realizing Grover's quantum search algorithm. First, a $Y_{\pi/2}$ pulse is applied to each qubit to produce the fully superposed state $1/2(|00\rangle + |01\rangle + |10\rangle + |11\rangle)$. Then, an iSWAP gate is applied, followed by a $Z_{\pm\pi/2}$ gate on each qubit, which corrsponds to the application of the oracle function. The resulting state is then analyzed using another iSWAP gate and two $Y_{\pi/2}$ gates to extract the state which has been marked by the oracle function. Optionally, a Y_π^{12} pulse is used on each qubit to increase the readout fidelity.

minimum of energy. When one initializes the system to a state $\psi_0(x, t_0)$ and lets it evolve for a given time, the resulting state $\psi(x, t)$ will have a tendency to have a high probability density in the local minimum of the potential, thus "falling" into the potential minimum much like a classical system would.

It is thus interesting to ask if one could encode the solution to some hard problem as a point of minimum energy x_0 of a potential $V(x)$ and design an algorithm that would take an initial state $\psi_0(x, t_0)$ and let it evolve into a state that has a high probability around x_0. Most problems in classical computer science involve functions operating on binary numbers of fixed length, so to encode these numbers we can discretize our wavefunction $\psi(x, t)$ using a regular grid of points x_i with a spacing dx, as shown in fig. **??**b. When we discretize the time evolution of eq. 7.1 in steps dt as well and define $\epsilon = dt/dx^2$, we obtain a new equation of the form

$$-\frac{\psi_i^{t+dt} - \psi_x^t}{dt} = \frac{\psi_{i+1}^t + \psi_{i-1}^t - 2\psi_x^t}{dx^2} - V(x_i)\psi_i^t \tag{7.2}$$

where we have written $\psi(x_i, t) = \psi_i^t$. This equation can be written in matrix form as

$$\vec{\psi}^{t+dt} = S^t \cdot \vec{\psi}^t \tag{7.3}$$

Grover algorithm

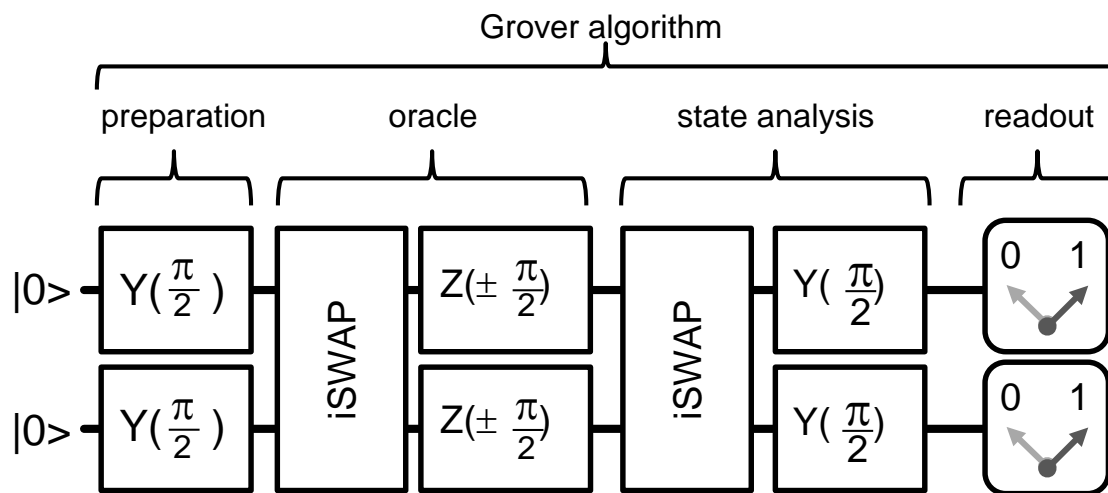| preparation | oracle | state analysis | readout |

Figure 7.2
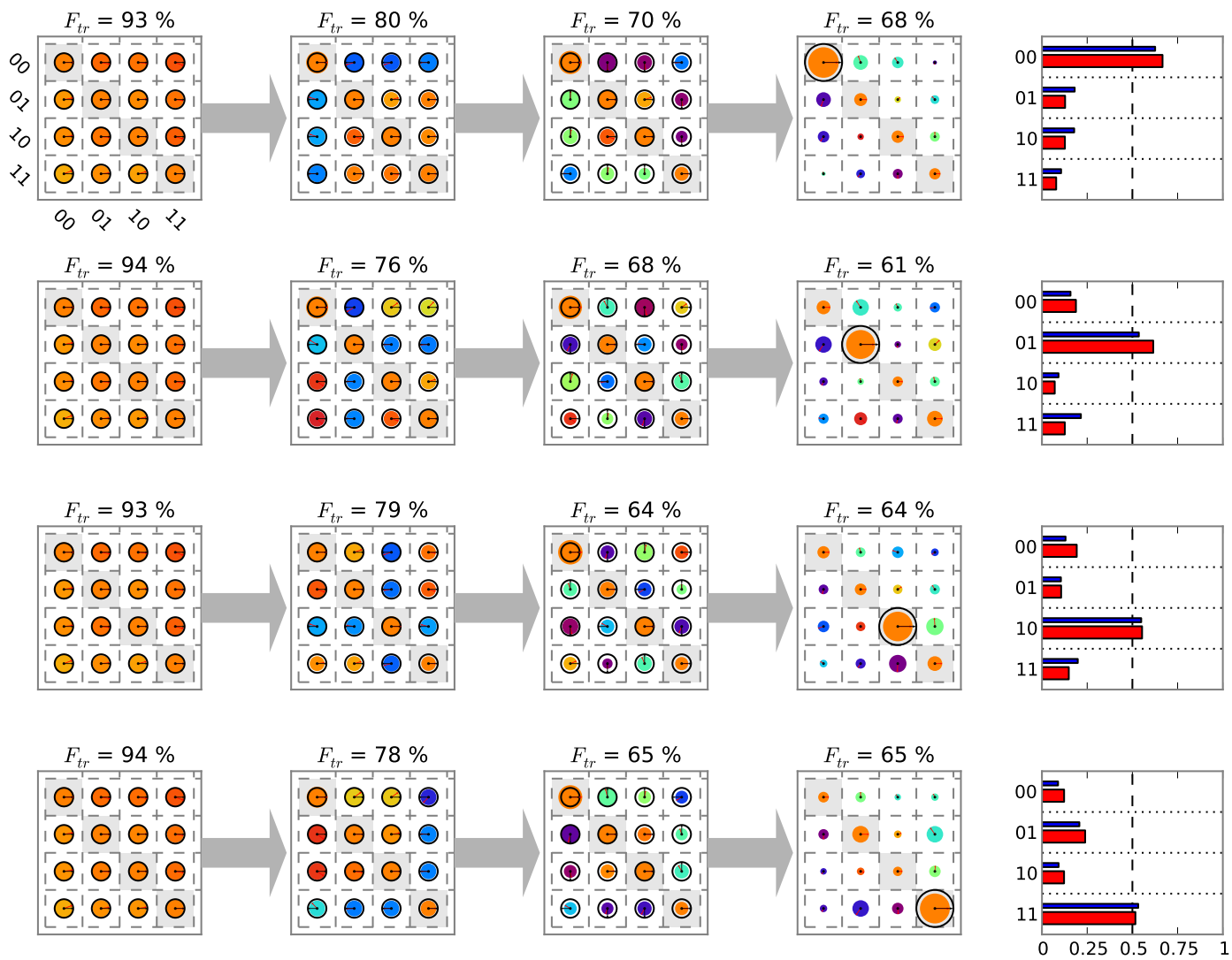
7.2 Experimental Implementation

7.3 Results

Figure 7.3
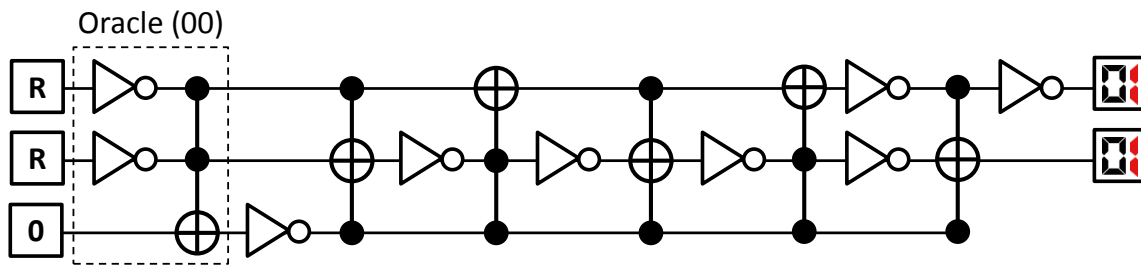
Figure 7.4: Classical reversible implementation of a search algorithm on a two-bit input register. The Oracle function can be implemented by two single-bit NOT operations and a Toffoli gate. R designates the generation of a random binary value at the beginning of the algorithm If the Oracle does not yield the correct answer, the test state gets incremented. The average success probability of the algorithm is 50 %.

7.3.1 Algorithm Fidelity

7.3.2 Single-Run Probabilities

7.3.3 Error Analysis

7.4 Conclusions

Chapter 8

Scalable Architectures for Quantum Bits

8.1 Definition & Requirements

8.2 Qubit Design

8.3 Microwave Driving

8.4 Frequency Manipulation

8.5 Readout

8.6 Coupling

8.7 A 4-Qubit Architecture

8.8 Scaling Up

Chapter 9

Conclusions & Outlook

9.1 Future Directions in Superconducting QC

9.1.1 3D Circuit Quantum Electrodynamics

9.1.2 Hybrid Quantum Systems

9.1.3 Quantum Error Correction & Feedback

Appendix A

Modeling of Multi-Qubit Systems

A.1 Analytical Approach

A.1.1 Multi-Qubit Hamiltonian

A.1.2 Energies and Eigenstates

A.2 Master Equation Approach

$$\frac{d\rho}{dt} = -\frac{i}{\hbar}[H,\rho] + \sum_j \left[2L_j \, \rho \, L_j^\dagger - \{L_j^\dagger L_j, \rho\} \right] \tag{A.1}$$

A.2.1 Direct Integration

A.2.2 Monte Carlo Simulation

A.2.3 Speeding Up Simulations

Appendix B

Data Acquisition & Management

B.1 Data Acquisition Infrastructure

B.2 Data Management Requirements

B.3 PyView

B.3.1 Overview

B.3.2 Instrument Management

B.3.3 Data Acquisition

B.3.4 Data Management

B.3.5 Data Analysis

Appendix C

Design & Fabrication

C.1   Mask Design

C.2   Optical Lithography

C.3   Electron Beam Lithography

Bibliography

Blais, A., Huang, R., Wallraff, A., Girvin, S. M., and Schoelkopf, R. J. (2004). Cavity quantum electrodynamics for superconducting electrical circuits: An architecture for quantum computation. *Physical Review A*, 69(6):062320.

Chiorescu, I., Nakamura, Y., Harmans, C. J. P. M., and Mooij, J. E. (2003). Coherent quantum dynamics of a superconducting flux qubit. *Science*, 299(5614):1869 –1871.

Clauser, J. F., Horne, M. A., Shimony, A., and Holt, R. A. (1969). Proposed experiment to test local Hidden-Variable theories. *Physical Review Letters*, 23(15):880–884.

Collin, E., Ithier, G., Aassime, A., Joyez, P., Vion, D., and Esteve, D. (2004). NMR-like control of a quantum bit superconducting circuit. *Physical Review Letters*, 93(15):157005.

Cottet, A. (2002). *Implementation of a quantum bit in a superconducting circuit*. PhD thesis, Université Paris VI, Paris.

DiCarlo, L., Chow, J. M., Gambetta, J. M., Bishop, L. S., Johnson, B. R., Schuster, D. I., Majer, J., Blais, A., Frunzio, L., Girvin, S. M., and Schoelkopf, R. J. (2009). Demonstration of two-qubit algorithms with a superconducting quantum processor. *Nature*, 460(7252):240–244.

DiCarlo, L., Reed, M. D., Sun, L., Johnson, B. R., Chow, J. M., Gambetta, J. M., Frunzio, L., Girvin, S. M., Devoret, M. H., and Schoelkopf, R. J. (2010). Preparation and measurement of three-qubit entanglement in a superconducting circuit. *Nature*, 467(7315):574–578.

DiVincenzo, D. P. (2000). The physical implementation of quantum computation. *Fortschritte der Physik*, 48(9-11):771–783.

Grover, L. K. (1997). Quantum mechanics helps in searching for a needle in a haystack. *Physical Review Letters*, 79(2):325–328.

Grover, L. K. (2001). From schrödinger's equation to the quantum search algorithm. *American Journal of Physics*, 69(7):769–777.

Haroche, S. and Raimond, J. (2006). *Exploring the Quantum: Atoms, Cavities and Photons*. Oxford University Press.

Koch, J., Yu, T. M., Gambetta, J., Houck, A. A., Schuster, D. I., Majer, J., Blais, A., Devoret, M. H., Girvin, S. M., and Schoelkopf, R. J. (2007). Charge-insensitive qubit design derived from the cooper pair box. *Physical Review A*, 76(4):042319.

Majer, J., Chow, J. M., Gambetta, J. M., Koch, J., Johnson, B. R., Schreier, J. A., Frunzio, L., Schuster, D. I., Houck, A. A., Wallraff, A., Blais, A., Devoret, M. H., Girvin, S. M., and Schoelkopf, R. J. (2007). Coupling superconducting qubits via a cavity bus. *Nature*, 449(7161):443–447.

Mallet, F., Ong, F. R., Palacios-Laloy, A., Nguyen, F., Bertet, P., Vion, D., and Esteve, D. (2009). Single-shot qubit readout in circuit quantum electrodynamics. *Nat Phys*, 5(11):791–795.

Martinis, J. M., Devoret, M. H., and Clarke, J. (1985). Energy-Level quantization in the Zero-Voltage state of a Current-Biased josephson junction. *Physical Review Letters*, 55(15):1543–1546.

Martinis, J. M., Nam, S., Aumentado, J., and Urbina, C. (2002). Rabi oscillations in a large Josephson-Junction qubit. *Physical Review Letters*, 89(11):117901.

Michael A. Nielsen and Isaac L. Chuang (2000). *Quantum Compuation and Quantum Information*. Cambridge University Press.

Mooij, J. E., Orlando, T. P., Levitov, L., Tian, L., van der Wal, C. H., and Lloyd, S. (1999). Josephson Persistent-Current qubit. *Science*, 285(5430):1036 –1039.

Nakamura, Y., Pashkin, Y. A., and Tsai, J. S. (1999). Coherent control of macroscopic quantum states in a single-Cooper-pair box. *Nature*, 398(6730):786–788.

Paik, H., Schuster, D. I., Bishop, L. S., Kirchmair, G., Catelani, G., Sears, A. P., Johnson, B. R., Reagor, M. J., Frunzio, L., Glazman, L. I., Girvin, S. M., Devoret, M. H., and Schoelkopf, R. J. (2011). Observation of high coherence in josephson junction qubits measured in a Three-Dimensional circuit QED architecture. *Physical Review Letters*, 107(24):240501.

Palacios-Laloy, A. (2010). *Superconducting qubit in a resonator: Test of the Leggett-Garg inequality and single-shot readout*. PhD thesis, Université Paris VI, Paris.

Siddiqi, I., Vijay, R., Metcalfe, M., Boaknin, E., Frunzio, L., Schoelkopf, R. J., and Devoret, M. H. (2006). Dispersive measurements of superconducting qubit coherence with a fast latching readout. *Physical Review B*, 73(5):054510.

Siddiqi, I., Vijay, R., Pierre, F., Wilson, C. M., Metcalfe, M., Rigetti, C., Frunzio, L., and Devoret, M. H. (2004). RF-Driven josephson bifurcation amplifier for quantum measurement. *Physical Review Letters*, 93(20):207002.

Vijay, R., Devoret, M. H., and Siddiqi, I. (2009). Invited review article: The josephson bifurcation amplifier. *Review of Scientific Instruments*, 80(11):111101–111101–17.

Vijay, R., Slichter, D. H., and Siddiqi, I. (2011). Observation of quantum jumps in a superconducting artificial atom. *Physical Review Letters*, 106(11):110502.

Vion, D., Aassime, A., Cottet, A., Joyez, P., Pothier, H., Urbina, C., Esteve, D., and Devoret, M. H. (2002). Manipulating the quantum state of an electrical circuit. *Science*, 296(5569):886 –889.

Wallraff, A., Schuster, D. I., Blais, A., Frunzio, L., Huang, R.-S., Majer, J., Kumar, S., Girvin, S. M., and Schoelkopf, R. J. (2004). Strong coupling of a single photon to a superconducting qubit using circuit quantum electrodynamics. *Nature*, 431(7005):162–167.